# SILIKÁTNIK 2025

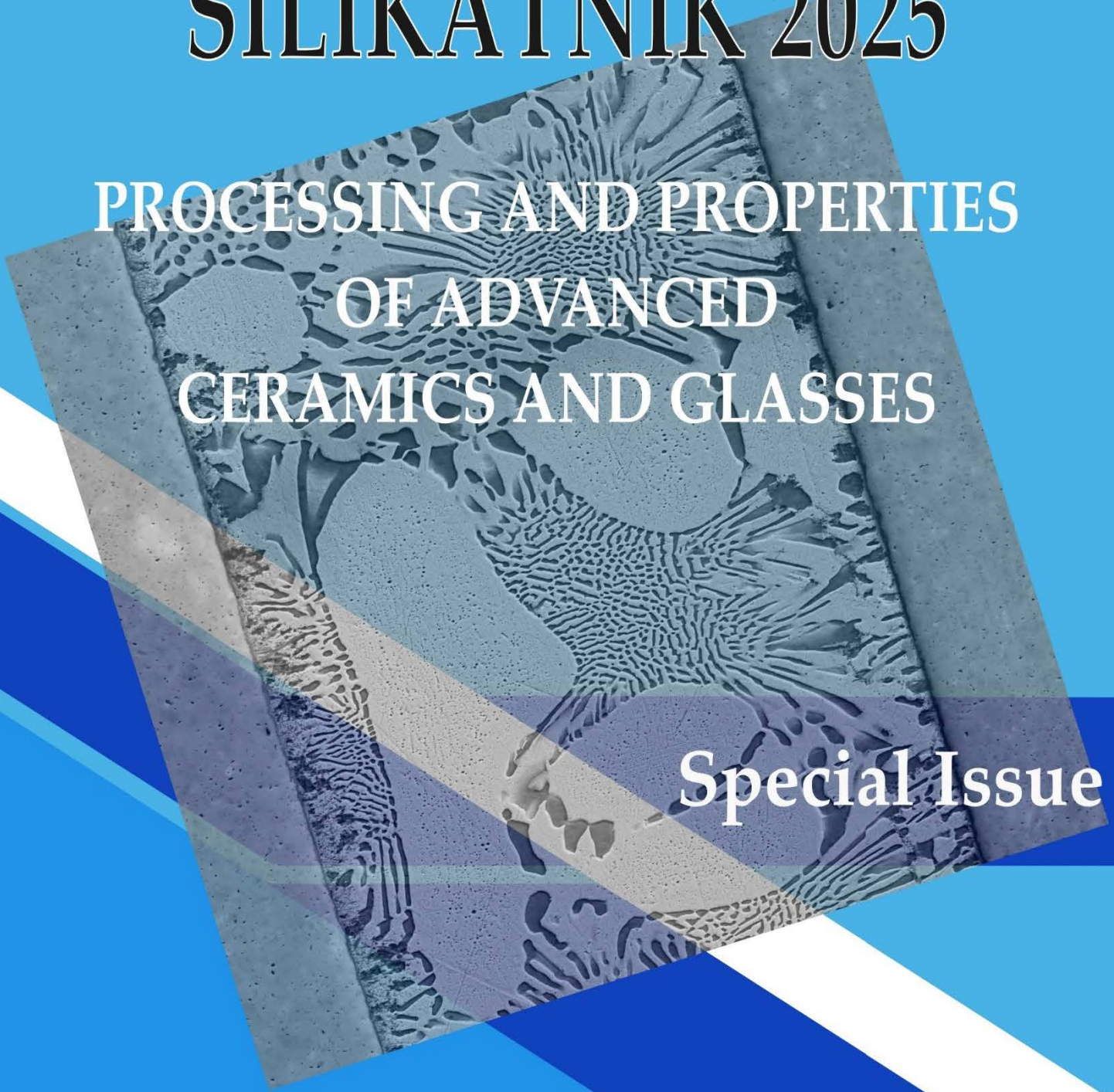

## PROCESSING AND PROPERTIES OF ADVANCED CERAMICS AND GLASSES

**Special Issue**

Slovak Silicate Scientific - Technological Society

ISBN 978–80–975243–0–2

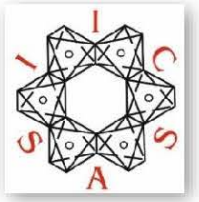


Institute of Inorganic Chemistry,
Slovak Academy of Sciences

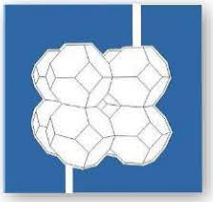

Slovak Silicate Scientific-
Technological Society


Slovak Academy of Sciences

## SCIENTIFIC BOARD

prof. RNDr. Ján Dusza, DrSc.
prof. Ing. Dušan Galusek, DrSc.
prof. RNDr. Pavol Šajgalík, DrSc

## REVIEWERS

prof. Ing. Marián Janek, PhD.
Ing. Ondrej Hanzel, PhD.
Ing. Martin Michálek, PhD.

*Silikátnik 2025, Special Issue*

# Enhancing thermoelectric performance of stabilized high-entropy perovskite ceramics through $Nb^{5+}$ substitution

Asif Ali[1,*], Monika Tatarková[1], Vladimir V. Srdić[2], Nikola Kanas[3], Ondrej Hanzel[1], Peter Tatarko[1]

[1]*Institute of Inorganic Chemistry, Slovak Academy of Sciences, Dubravska cesta 9, 845 36 Bratislava, Slovak Republic*
[2]*Department of Materials Engineering, Faculty of Technology Novi Sad, University of Novi Sad, Bul. Cara Lazara 1, 21000, Novi Sad, Serbia*
[3]*TEGMATICA Ltd, Karlovacki drum 32, 23300, Kikinda, Serbia*
**asif.ali@savba.sk*

## ABSTRACT

Novel high-entropy stabilized perovskite oxides, $Sr_{0.25}Ba_{0.25}Ca_{0.25}La_{0.25}Ti_{1-x}Nb_xO_3$ with varying $Nb^{5+}$ concentrations, were successfully synthesised using the conventional solid-state route and sintered by spark plasma sintering. The XRD and Raman spectra confirmed the formation of a single-phase simple cubic perovskite structures in all materials. SEM and EDX analysis confirmed the dense microstructures and homogeneous distribution of host elements with a relative density > 95 %. The increase in configuration entropy of samples had a significant impact on the thermoelectric performance. The sample possessed a negative Seebeck coefficient (S), confirming its n-type semiconducting behavior. Along with that, the sample exhibited a low thermal diffusivity of < 1 $mm^2/s$, low thermal conductivity (K) value < 3.8 $Wm^{-1}K^{-1}$, and moderate electrical conductivity $\sigma \sim 126$ S/m. The present work offers a compositional design approach for perovskite oxides to reduce their intrinsic thermal conductivity and enhance their thermoelectric performance.

**Keywords:** thermoelectrics, high-entropy ceramics, perovskite oxides, thermal conductivity, power factor

## INTRODUCTION

The demand for green and sustainable energy is increasing day by day with the growing needs of the world. This is ultimately related to the global energy crisis. This persuades the researcher to explore new ways to facilitate the efficiency and diversity of energy utilization. Renewable sources, such as solar, wind, and geothermal, have been utilized to replace fossil fuels to reduce global warming and air pollution [1]. Thermoelectric (TE) device is composed of multiple pairs of p-type and n-type semiconductor legs, which are electrically connected in series to increase the output voltage and thermally connected in parallel to ensure efficient heat flow between the hot and cold sides. When a temperature gradient is applied across the module, charge carriers in each leg diffuse from the hot side to the cold side, generating an electrical potential via the Seebeck effect. Such devices can significantly contribute to the challenges of the global energy crisis [2]. The state-of-the-art TE materials are tellurides $Bi_2Te_3$ and PbTe; however, they possess insufficient stability at temperatures above 300 °C in air This paves the way for oxides that are stable at high temperatures (up to 800 °C) and more environmentally friendly. Perovskite oxides with the $ABO_3$ structure are considered promising candidates for TE applications [3]. $SrTiO_3$ (STO) is an attractive material for TE applications, due to its peak dimensionless figure of merit (ZT) value ~ 0.6 [4] at high temperatures (1000 - 1100 K). The dimensionless figure of merit ZT is defined as $ZT = S^2\sigma T/K$, where S, σ, T, and K represent the Seebeck coefficient (thermoelectric power), electrical conductivity, absolute temperature,

and thermal conductivity, respectively. The ZT value is used to represent the efficiency of TE materials in converting heat into electricity. One of the significant drawbacks of STO for TE applications is its high thermal conductivity at room temperature (K = 12 $W.m^{-1}K^{-1}$), whereas a much lower K = $1W.m^{-1}K^{-1}$ is required to achieve a high ZT value [5].

Over the last few decades, researchers have adopted several techniques to minimize K of STO-based materials, such as the formation of nanostructured bulk materials and superlattices. The concept of high entropy in ceramic perovskites brought a breakthrough in the field of TE, as the versatile perovskite structure ($ABO_3$) can accommodate multiple cations at the A and/or B sites [6]. The concept of high entropy oxides (HEO) was introduced by Rose et al. [7] for the first time in 2015 by synthesizing five principal metal cations' single-phase crystal structure in a near equimolar ratio. Later in 2016, the idea of HEO was extended to design high entropy perovskites (HEPOs) using four or more principal metal cations in near equimolar ratios and having a single-phase crystal structure. Due to structural disorder and local distortions, these materials exhibit superior thermal and electrical properties with notably low K < 1.09 W/m.K at 923 K[8] , which is crucial for enhancing ZT value. Donor $Nb^{5+}$ substitution at the Ti-site was reported to lower the K < 2.3 W/m.K at 873 K by inducing additional defects in the crystal lattice of the pristine STO structure [9]. These complex defects disrupt the regular lattice structure, leading to an increase the phonon scattering, which ultimately lowers the K, but the effect of Nb doping has not yet been investigated for HE compositions.

Therefore, the main aim of the present work is to design and synthesize novel high-entropy perovskite oxides (HEPOs) for sustainable energy, i.e. $Sr_{0.25}Ba_{0.25}Ca_{0.25}La_{0.25}Ti_{1-x}Nb_xO_3$ with $x$ = 0, 0.005, 0.01, and 0.05. The HEPOs with varying $Nb^{5+}$ concentration was synthesized via solid-state reaction method. The chemical compositions were designed based on initial calculations, considering tolerance factor, electronegativity, polarizability, charge neutrality, configurational entropy, and global instability index using SPUD (structure prediction diagnostic software).

## EXPERIMENTAL SECTION

$Ba_{0.25}Ca_{0.25}Sr_{0.25}La_{0.25}Ti_{1-x}Nb_xO_3$ ($x$ = 0.005, 0.01, 0.03, and 0.05) ceramics were synthesized via a solid-state route and sintered using field-assisted sintering technology (FAST). Reagent-grade raw precursors $BaCO_3$, $CaCO_3$, $La_2O_3$, $SrCO_3$, $TiO_2$, and $Nb_2O_5$, with a purity of > 99 % (supplied by Sigma Aldrich), were dried in an oven, and weighed according to the molar stoichiometric ratio. The powder mixtures were then subjected to planetary ball milling (PM100, Retsch) for 2 h at a speed of 250 rpm with a ball-to-powder ratio of 6:1. The dried powders were then calcined in a closed alumina crucible using a muffle at 1100 °C for 4 h at the heating and cooling rate of 5 and 10 °C/min, respectively. The calcined powders were then placed in a graphite die with an inner diameter of 20 mm, and sintered using a FAST machine (DSP 507, Dr. Fritsch) at 1200 °C with a dwell time of 3 min, while the heating and cooling rates were 100 and 50 °C /min, respectively. The sintered samples had a diameter of 20 mm and a thickness of 4 mm. For the electrical measurements, the samples were cut into rectangular bars of approximately (4 × 4 × 15 mm).

The crystalline phases of the ceramic samples were analyzed by X-ray diffractometer (PANalytical X'pert pro) with CuKα radiation (λ = 1.5406 Å). Raman spectra were collected using the Raman microscope multichannel Renishaw In, Via Reflex micro spectrometer. The electrical conductivity (σ) along with the Seebeck coefficient (S) was measured on the bulk rectangular bar samples using the in-plane van der Pauw method in a cross configuration. These measurements were done using the proboStat™ measurement cell (NorECs AS, Germany). The data were collected over the temperature range of 200 – 900 °C in 5 % $H_2$/Ar atmosphere, using a heating and cooling rate of 200°C/ h, respectively, with a step size of 100 °C, and a dwell time

of 3 h at each step. A differential scanning calorimeter (NETZSCH STA 449C, Germany) was used to obtain the specific heat capacity (Cp), and sapphire was selected as a standard sample for the calibration. The thermal diffusivity (α) was determined by a laser flash method (Linseis LFA 1000, Germany). Based on the fundamental parameters of thermal diffusivity (α), specific heat ($C_p$), and bulk density (ρ), the total thermal conductivity (K) was calculated as $K = \rho\alpha Cp$.

## RESULTS AND DISCUSSION

### Phase analysis

The X-ray diffraction patterns of the sintered high-entropy perovskite oxides are shown in **Fig. 1(a)**. The lattice parameters (a, b, c) and interplanar d-spacing of the sample matched with PDF # 31-174, confirming the cubic structure with a space group Pm-3m for all the samples. No detectable traces of secondary phases were observed within the detection limits of the present setup. A slight shift of the (100) reflection toward the lower 2θ was observed compared with the cubic perovskite $CaTiO_3$ (PDF # 43-0226). The shift can be attributed to the smaller ionic radii of the B-site cations compared with the average ionic radii of $Ba_{0.25}Ca_{0.25}Sr_{0.25}La_{0.25}Ti_{1-x}Nb_xO_3$ ($x = 0$) ceramics (1.438 Å) [10].

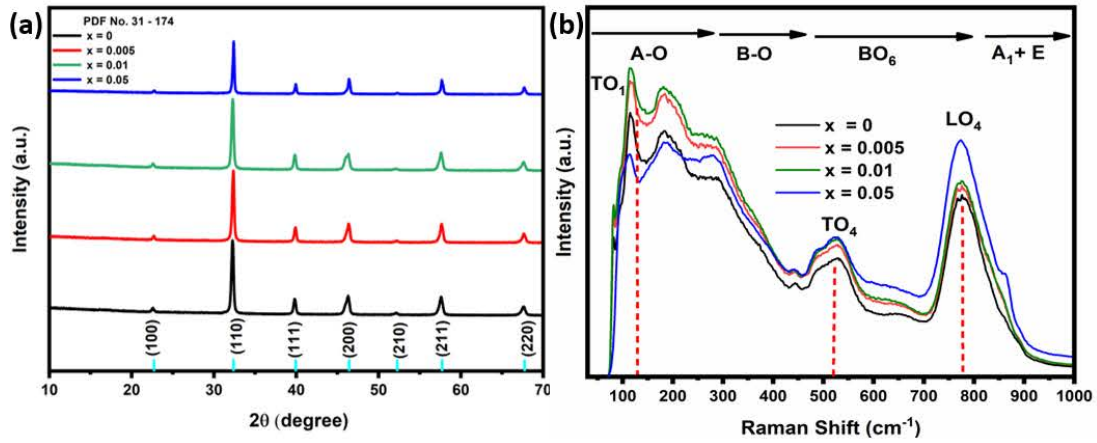


*Fig. 1 (a) X-ray diffraction patterns and (b) Raman spectra of Ba0.25Ca0.25Sr0.25La0.25Ti1-xNbxO3 high-entropy ceramics samples x = 0.05*

Raman spectra of the samples (**Fig. 1(b)**) revealed structural disorder and local symmetry changes in HEPO ceramics. The presence of the bands at the lower wavenumber is not typically reported for pure STO [11]. Therefore, the presence of such a band in the spectra of the samples suggests a deviation from the Raman selection rule [12] and is associated with the $TO_1$, $TO_4$, and $LO_4$ phonon modes, respectively. The low-frequency band < 200 $cm^{-1}$ is attributed to the A-site cation - oxygen vibration, involving bonds, such as Ca-O, Sr-O, La-O, and Sr-O bonds [13]. These bands appear as Raman-active in the spectra due to the breaking of central symmetry, defects, and strain. The bands in the 200 – 400 $cm^{-1}$ range are associated with the vibration of B-site cations and B-O bonds, including the Ti-O and Nb-O bonds [14]. Additionally, the band observed at 543 $cm^{-1}$ corresponds to the vibration of $TiO_6$ octahedra [13].

The SEM micrographs of the HEPO samples are shown in **Fig. 2**. All the samples showed a relative density > 95 %. The microstructures consisted of irregular grain morphologies with distinct grains, while a decrease in the apparent grain size < 2.7 μm for $x = 0.05$ was observed for the increase in $Nb^{5+}$ concentration. The reason for the reduction of the grain size can be attributed to the presence of vacancies, as the presence of the oxygen vacancies inhibits the grain growth by acting as pinning sites [15]. The EDS analysis results presented in **Fig. 2**

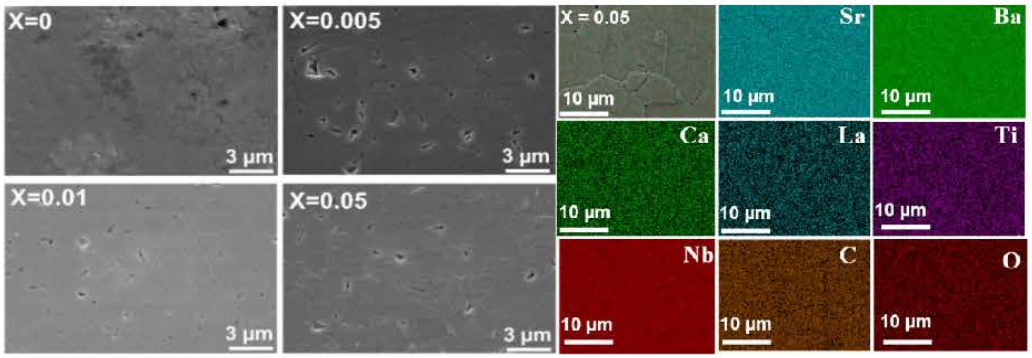


*Fig. 2 SEM of $Ba_{0.25}Ca_{0.25}Sr_{0.25}La_{0.25}Ti_{1-x}Nb_xO_3$ high-entropy ceramics with varying Nb content. EDS result for the sample with x = 0.05*

demonstrated that the multicomponent elements of Sr, Ca, Ba, La, Ti, and Nb were uniformly distributed, and their atomic percentage conforms to the designed high-entropy composition.

## Thermal diffusivity and thermal conductivity

Thermal diffusivities and thermal conductivities of the samples are shown in **Fig. 3**. Both showed a decreasing trend with temperature, in accordance with scattering governed by the mean free path of the phonons (a = 1/T proportionality). Furthermore, the sample with $x = 0.005$ showed the lowest thermal conductivity among of all the investigated samples, which can be attributed to the lower grain size of this sample 2.9 μm.

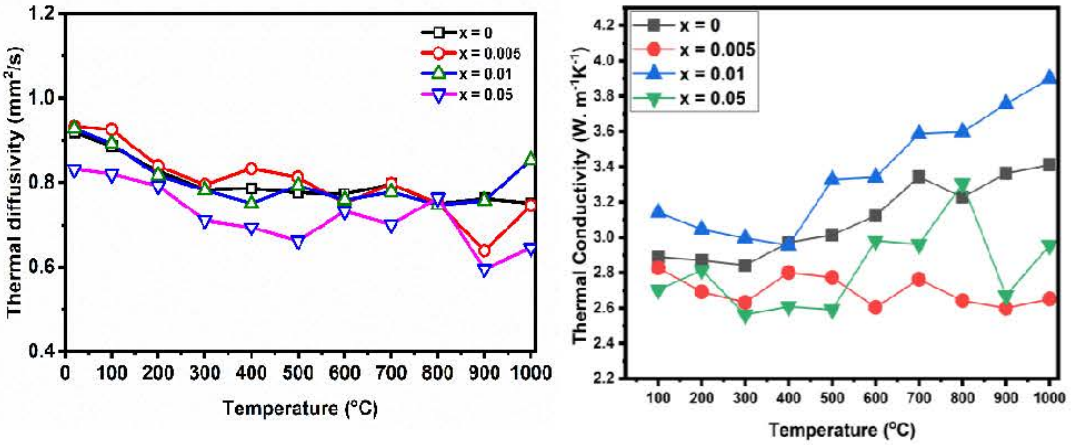


*Fig. 3 a) Thermal diffusivity and b) thermal conductivity of $Ba_{0.25}Ca_{0.25}Sr_{0.25}La_{0.25}Ti_{1-x}Nb_xO_3$ high-entropy ceramics with varying Nb content*

## Seebeck analysis

The thermoelectric performance of the HEPO samples was evaluated by their Seebeck coefficient and electrical conductivity, as shown in **Fig. 4**. All the prepared samples exhibited negative Seebeck values, indicating the n-type thermoelectric behaviour, which monotonically increased with increasing temperature. The Seebeck coefficient is sensitive to carrier concentration, electron density, and effective mass. It also depends on the electronic structure near the Fermi energy level. The variation in S was in the range from approximately −164 μV $K^{-1}$ to −316 μV $K^{-1}$. The two main factors that determine the S are the effective mass (m*) and carrier concentration (n). For metals or degenerate semiconductors, the relationship between S and carrier concentration n [16] is given by:

$$S = \frac{8\pi^2 K^2 B}{3eh^2} m^* T \left(\frac{\pi}{3n}\right)^{2/3} \qquad (1)$$

where e, h, and $m^*$ represent the electron charge, Planck's constant, and effective mass, respectively. In addition, $K_B$ denotes the Boltzmann constant and T is the absolute temperature. In general, doping/substitution is used to tune the effective mass. A higher density- of - states effective mass generally results in a large absolute S. Moreover, an increase in effective mass ($m^*$) is often due to the flattening of the conduction band, which is associated with an increase in the bandgap (Eg), as described by the Kane dispersion relation [17].

$$\frac{hK^2}{2m^*} = E\left(1 + \frac{E}{Eg}\right) \qquad (2)$$

In equation (2), the effective mass increases with increasing bandgap. Hence, |S| is inversely proportional to the carrier concentration $(n)^{-2/3}$. The observed decrease in the value of the Seebeck coefficient with increasing concentration of $Nb^{5+}$ is attributed to the increase in the carrier concentration. According to the Mott relation, the Seebeck coefficient is inversely related to carrier concentration (holes in p-type and electrons in n-type materials).

**Electrical conductivity**

The electrical conductivity of the samples presented in **Fig. 4 (b)** confirmed that they exhibited semiconductor behaviour. In semiconductor materials, mostly the vacancies and Schottky complex defects can stably exist in the materials within a specific temperature range, acting as charge carriers to enhance the electrical conductivity. Generally the electrical conductivity increases with temperature up to a critical point, then decreases as lattice vibrations disrupt defects. Strong electronegativity keeps electrons localized, limiting conductivity. Another reason for the relatively low conductivity in TE pervoskite oxides is the limited overlap of atomic orbitals due to the smaller atomic radii [18]. The electrical conductivity increased with increasing temperature as well as with varying $Nb^{5+}$ concentration. This is associated with the aliovalent nature of $Nb^{5+}$ dopnat at the B-site cause an induced oxygen vaccancies.

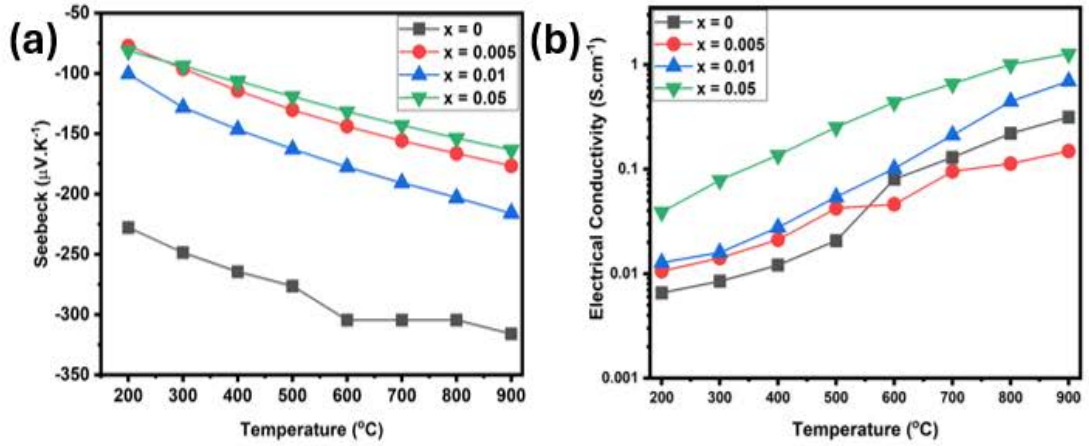


***Fig. 4*** *(a) Temperature dependence of Seebeck coefficient (b) Electrical conductivity of entropy stabilised perovskite oxides*

**Power factor (P = S2σ)**

The power factor as a function of temperature for all samples is shown in **Fig. 5**. It is a critical parameter for evaluating the performance of thermoelectric materials, as it reflects the balance between the Seebeck coefficient and electrical conductivity. The increasing $Nb^{5+}$ concentration at the $Ti^{4+}$ site of the perovskite structure, S decreased while the electrical conductivity increased. This is consistent with the well-known trade-off between these two properties. Despite the reduction in S, the increase in conductivity compensated and enhanced the overall power factor.

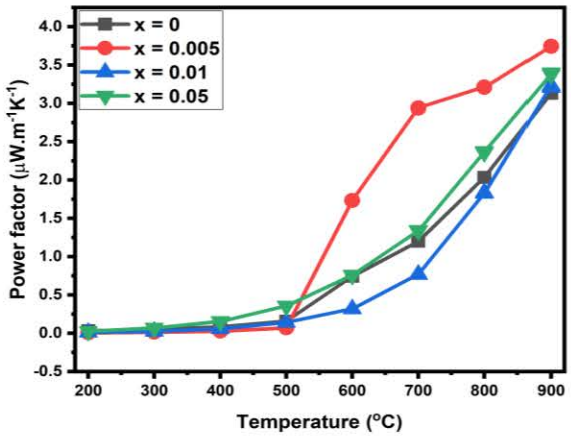


***Fig. 5*** *Power factor of the entropy stabilised perovskite oxides as function of temperature*

## CONCLUSIONS

Novel configurational high-entropy perovskite oxides $Ba_{0.25}Ca_{0.25}Sr_{0.25}La_{0.25}Ti_{1-x}Nb_xO_3$ with varying $Nb^{5+}$ concentration were successfully synthesized via a solid-state route. XRD analysis confirmed the formation of the single-phase cubic symmetry. Further, the local structure confirmation was carried out through a Raman spectrometer. The SEM analysis confirmed the formation of relatively dense microstructures. The thermal diffusivity and thermal conductivity were significantly reduced with the addition of $Nb^{5+}$, which acted as a point defect to scatter phonons. All the compositions exhibited a negative Seebeck coefficient. The carrier mobility was enhanced with the introduction of $Nb^{5+}$, which resulted in the improvement of electrical conductivity. Consequently, the power factor was improved considerably. This work provides a new strategy by using high-entropy engineering for composition design in perovskite oxides for TE applications.

## ACKNOWLEDGMENT

This work was funded by the EU NextGenerationEU through the Recovery and Resilience Plan for Slovakia under the project No. 09I03-03-V03-00094/2024/VA.

## REFERENCES

1. X.-L. Shi, J. Zou, Z.-G. Chen, Advanced thermoelectric design: from materials and structures to devices. Chemical reviews 120, 7399-7515 (2020)
2. P. Zhang et al., Reduced lattice thermal conductivity of perovskite-type high-entropy (Ca0. 25Sr0. 25Ba0. 25RE0. 25)TiO3 ceramics by phonon engineering for thermoelectric applications. Journal of Alloys and Compounds 898, 162858 (2022)

3. P. Zhang et al., High-entropy (Ca0.2Sr0.2Ba0. 2La0. 2Pb0. 2)TiO3 perovskite ceramics with A-site short-range disorder for thermoelectric applications. Journal of Materials Science & Technology 97, 182-189 (2022)
4. Y. Zhu et al Electronic transport and the thermoelectric properties of donor-doped SrTiO3. Journal of Physics: Energy 6, 025027 (2024)
5. P. Zhang et al., High-entropy (Ca0. 2Sr0. 2Ba0. 2La0. 2Pb0. 2)TiO3 perovskite ceramics with A-site short-range disorder for thermoelectric applications. Journal of Materials Science & Technology 97, 182-189 (2022)
6. R. Muhammad, A. Ali, J. Camargo, M. S. Castro, D. Han, Influence of Ti-vacancies on the site occupancy of amphoteric calcium, oxygen vacancies, dielectric, optical, and ferroelectric behavior of Ba0. 8Ca0. 2Ti1-xO3-δ. Journal of Alloys and Compounds 1010, 178115 (2025)
7. C. M. Rost et al., Entropy-stabilized oxides. Nature communications 6, 8485 (2015).
8. Y. Zheng et al., Electrical and thermal transport behaviours of high-entropy perovskite thermoelectric oxides. Journal of Advanced Ceramics 10, 377-384 (2021)
9. Q.-Q. Fu, et al., Controlling the A-site deficiency and oxygen vacancies by donor-doping in pre-reductive-sintered thermoelectric SrTiO3 ceramics. Acta Materialia 229, 117785 (2022)
10. R. Muhammad, A. Ali, J. Camargo, M. S. Castro, Temperature stable dielectric properties in BaTiO3–Bi (Mg2/3Nb1/3) O3–NaNbO3 solid solution. ChemistrySelect 5, 3730-3734 (2020)
11. Y. I. Yuzyuk, Raman scattering spectra of ceramics, films, and superlattices of ferroelectric perovskites: A review. Physics of the Solid State 54, 1026-1059 (2012)
12. Y. I. Yuzyuk, Raman scattering spectra of ceramics, films, and superlattices of ferroelectric perovskites: A review. Physics of the Solid State 54, 1026-1059 (2012)
13. D. A. Fernandez-Benavides et al., Comparative study of ferroelectric and piezoelectric properties of BNT-BKT-BT ceramics near the phase transition zone. Materials 11, 361 (2018)
14. F. Cheng et al., Ti4+-incorporated fluorite-structured high-entropy oxide (Ce,Hf,Y,Pr,Gd)O2− δ: optimizing preparation and CMAS corrosion behavior. Journal of Advanced Ceramics 11, 1801-1814 (2022)
15. P. Jaiban, A. Watcharapasorn, R. Yimnirun, R. Guo, A. S. Bhalla, Effects of donor and acceptor doping on dielectric and ferroelectric properties of Ba0.7Ca0.3TiO3 lead-free ceramics. Journal of Alloys and Compounds 695, 1329-1335 (2017)
16. X.-L. Shi et al., SrTiO3-based thermoelectrics: Progress and challenges. Nano Energy 78, 105195 (2020)
17. Y. Pei, A. D. LaLonde, H. Wang, G. J. Snyder, Low effective mass leading to high thermoelectric performance. Energy & Environmental Science 5, 7963-7969 (2012)
18. H. Ohta et al., Giant thermoelectric Seebeck coefficient of a two-dimensional electron gas in SrTiO3. Nature materials 6, 129-134 (2007)

# Cytotoxicity and mechanical properties of hydroxyapatite-based composites for biomedical scaffolds

R. Fialka[1], Z. Chlup[2], Z. Varchulová Nováková[3], I. Vašková[4], Ľ. Danišovič[3], P. Veteška[1], P. Peciar[5] Ľ. Bača[1], M. Janek[1,6]

[1]*Department of Inorganic Materials, Faculty of Chemical and Food Technology, Slovak University of Technology, Radlinského 9, 81237 Bratislava, Slovakia*
[2] *Institute of Physics of Materials, Czech Academy of Sciences, Žižkova 513/22, 61600 Brno, Czech Republic*
[3]*Institute of Medical Biology, Genetics and Clinical Genetic, Faculty of Medicine, Comenius University, 81108 Bratislava, Slovakia*
[4]*Department of Plastics, Rubber and Fibres, Faculty of Chemical and Food Technology, Slovak University of Technology, 81237 Bratislava, Slovakia*
[5]*Institute of Process Engineering, Faculty of Mechanical Engineering, Slovak University of Technology, Námestie slobody 17, 81231 Bratislava, Slovakia*
[6] *Department of Physical and Theoretical Chemistry, Faculty of Natural Sciences, Comenius University, Mlynská dolina, Ilkovičova 6, CH1, 84215 Bratislava, Slovakia*

## ABSTRACT

This study investigated hydroxyapatite-based composites containing varying concentrations of talc as a potential sintering additive of hydroxyapatite (HA) for bone tissue applications. Samples were prepared by pressing of homogenised HA powders with 1, 5, and 10 wt. % talc admixtures. After pellet sintering at 1300 °C the cytotoxicity and mechanical testing were performed. Biocompatibility was assessed using MTT, LDH, and contact toxicity assays with ATSCs cells, showing no cytotoxic effects and no adverse influence on cell proliferation or membrane integrity. Mechanical characterization was carried out using the Vickers hardness test on samples stored 0, 3 and 6 weeks with cells in cultivation media. Results indicated that composites with 1 wt. % talc exhibited hardness comparable to pure hydroxyapatite, while a decrease was observed at 5 wt. %, followed by an increase at 10 wt. %. The hardness was influenced more strongly by talc concentration than by exposure to living cells. These findings demonstrate that hydroxyapatite-talc composites maintain biocompatibility while showing composition-dependent mechanical behaviour, highlighting their potential use in biomedical scaffold applications.

**Keywords:** hydroxyapatite, talc, cytotoxicity, Vickers hardness

## INTRODUCTION

Hydroxyapatite ($Ca_5(PO_4)_3OH$) represents the principal inorganic constituent of human bone and teeth. Research into its application in tissue engineering began in the 1950s, and since that time, the hydroxyapatite as a candidate material for bone implants and substitutes has been extensively investigated [1]. Because of its close resemblance to the mineral phase of bone and its exceptional osteoconductive properties, synthetic hydroxyapatite has frequently been employed in bone grafting. Compared with bioactive glass, particularly borate-based varieties, hydroxyapatite exhibits superior biocompatibility and offers greater mechanical strength than many other bioactive glasses and certain calcium phosphates [2].

Talc, $Si_4Mg_3O_{10}(OH)_2$, is a natural compound belonging to the group of layered silicate minerals, widely used in the form of a fine powder in several industrial products such as ceramics, sealants, ignition retardants and as an active filler in polymer/silicate composites to

improve mechanical properties (e.g. strength, elasticity, impact resistance, etc.) and polymer nucleation. The structure of talc consists of the well-known 2:1 layer having T-O-T configuration. There are two tetrahedral (T) sheets containing Si as tetrahedron central atoms and an octahedral (O) sheet with Mg as octahedron central atoms. The octahedral sheet is sandwiched between the two tetrahedral sheets. The structure of talc does not exhibit a residual surface charge as known for some other layered silicates and the bonds between the layers are provided by weak electrostatic and Van der Waals forces [3]. According to literature, the incorporation of talc can significantly improve the mechanical properties of HA without reducing biocompatibility [4]. On the other hand, studies on the biocompatibility of talc and medical applications such as drug delivery systems are scarce and have been published relatively recently [5].

The contemporary approach in orthopedics and dental surgery where the implantation involves the application of scaffolds as bone replacement into fractured or otherwise compromised bone tissue, is the main focus of this study. The scaffolds, whether of natural or synthetic origin, provide a supportive framework that facilitates cell attachment and proliferation. The interconnected porosity of the material promotes cell migration as well as the effective transport of oxygen, nutrients, and metabolic waste, enabling bone tissue to regenerate from the periphery toward the interior of the implant. To achieve suitable porosity that would enable also scaffolds vascularisation recently been fabricated using 3D printing techniques [6].

The goal of this work was to fabricate a series of hydroxyapatite-based composite materials containing talc admixture and evaluate their potential for biomedical applications by characterizing their cytotoxicity and mechanical properties.

## EXPERIMENTAL

The main component of the pellets was commercially available as powdered calcium deficient hydroxyapatite of pharmaceutical grade, whose molar ratio Ca/P was 1.53. Samples were prepared from pure hydroxyapatite, as well as with an admixture of talc in concentrations of 1, 5 and 10 wt. %. Subsequently, the powder mixtures were homogenized and pressed on a uniaxial press at a pressure of 4 MPa, thereby preparing pellets with a diameter of 12 mm and a weight of 0.5 g. After pressing, the pressed pellets were heated in a muffle furnace using heating rate of 10 °C per minute to a holding temperature of 1300 °C, at which they were sintered for 1 hour.

The cytotoxicity of the prepared materials was evaluated by the MTT and LDH method. The MTT method is based on the reduction of yellow 3-(4,5-dimethylthiazol-2-yl)-2,5-diphenyltetrazolium bromide (MTT) into insoluble formazan (blue star-shaped crystals). The reaction takes place on the mitochondrial membrane of living cells. The formazan was dissolved by adding detergent and the coloration was evaluated spectrophotometrically using an ELISA reader at a wavelength of 490 nm.

A test for lactate dehydrogenase (LDH, cell death due to damage to the cell membrane) to evaluate the material was also used. This method is sensitive to cell membrane integrity due to LDH release into the culture medium through damaged cell membranes. When the cytoplasmic membrane is disrupted, LDH is rapidly released into the cell culture supernatant.

For the contact toxicity test, 3 parallel experiments were performed with each sample. Cell morphology was examined in an inverted microscope after 48 and 72 hours. After reaching confluence in the negative control without matrix (72h), the experiment was terminated, the cells in the Petri dishes were passaged and counted using a Bürker counting chamber. In this experiment, a cell suspension with a concentration of 50,000 cells per 1 ml in DMEM supplemented with fetal serum and antibiotics was used. A Petri dish with cells without matrix,

with sterile gauze and a sample of unmodified HA served as negative controls. A sterile gauze with 20 % sodium dodecyl sulfate (SDS) solution served as positive control. 1ml of cell suspension was added to the samples in Petri dishes and then 5ml of DMEM. The Petri dishes were held in an incubator with a temperature of 37 °C and a 6 % $CO_2$ atmosphere.

Before the mechanical testing, samples intended for hardness evaluation were stored in contact with adipose tissue-derived stromal cells (ATSCs) under controlled culture conditions. Prior to seeding, the materials were rinsed several times with 5–10 mL of phosphate-buffered saline (PBS) and subsequently sterilized under UV light for 30 minutes on each side. Following sterilization, ATSCs cells were seeded onto the prepared materials. For each well of a 24-well plate containing the samples, a cell suspension was pipetted to achieve a final cell concentration of $7 \times 10^3$ cells per well per material.

The samples with attached cells were monitored using an inverted microscope throughout the cultivation period. The culture medium was replaced three times per week for the duration of the experiment (3 and 6 weeks). After completion of the 6-week incubation, the cells were detached from the material using 0.25 % trypsin and rinsed with 5–10 mL of PBS. The samples were then dried and prepared for subsequent mechanical testing.

The mechanical characterization included the Vickers hardness test. This method employs a diamond pyramid indenter pressed into the polished surface of the sample under a defined load. The diagonals of the resulting indentation are measured using optical microscopy, and the Vickers hardness value (HV) is calculated as the applied load divided by the surface area of the indentation tip. This standardized test provides a reliable measure of the material's resistance to localized plastic deformation. For our experiment a screw driven testing machine ZWICK Z2.5 equipped with micro hardness head ZHU0.2 with built-in optical unit was used. For the test, samples that had been in contact with living cells for three and six weeks were compared with control samples that had not been exposed to cells.

For each sample, at least ten indentations were made at defined intervals to ensure that individual impressions did not influence one another due to stress field overlap. This approach also allowed the assessment of potential surface heterogeneities by covering a larger area of each sample. The mean Vickers hardness (HV) value was calculated from all statistically valid measurements.

## RESULTS

The cytotoxic response of the sintered samples was assessed on the ATSCs cell line using the MTT assay. Results indicated no cytotoxic effect after 48 hours. When the data were expressed in terms of cell proliferation, values remained above 75 %. To further evaluate cytotoxicity, the LDH assay was performed by collecting the culture supernatant and measuring LDH activity calorimetrically. The findings demonstrated that the material did not compromise plasma membrane integrity, as any toxic effect would have resulted in immediate LDH release, which was not observed. None of the samples showed a significant adverse effect on cell proliferation and morphology in the contact toxicity test either.

The results of the Vickers hardness are shown in **Fig. 1**. The test showed that composites containing 1 wt % admixture of talc reach Vickers hardness comparable to that of unmodified hydroxyapatite. An interesting trend has been observed, where the Vickers hardness significantly decreases in samples containing 5 wt % of talc, but increases again with 10 wt % of the admixture. The results also show that the length of contact with living cells was statistically less impactful on the Vickers hardness of the samples compared to the effect of the concentration of talc.

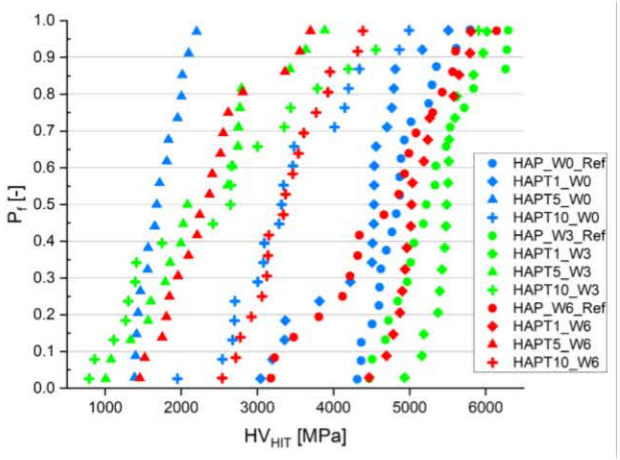


***Fig. 1*** *Vickers hardness of the sintered pellets with concentration 1 wt %, 5 wt % and 10 wt % of talc after contact with living cells for the duration of 0, 3 and 6 weeks*

## CONCLUSIONS

The goal of our work was to evaluate hydroxyapatite-based composite material and its suitability for biomedical applications. Its cytotoxicity was analysed using MTT and LDH tests, displaying no cytotoxic effect after 48 hours in the case of the former and no negative effects on the cells' plasmic membrane using the latter method. Likewise, no negative effect was observed during contact toxicity test after 48 and 72 hours. The Vickers hardness test revealed that composites with 1 wt % talc displayed hardness comparable to pure hydroxyapatite, while hardness decreased at 5 wt % and increased again at 10 wt %. Overall, talc amount added to the HA had a stronger influence on hardness than was the exposure time to living cells we used.

## ACKNOWLEDGMENT

The financial support of Slovak Grant Agency VEGA (grant No. VEGA 1/0070/22) and of the Slovak Research and Development Agency under Contract No. APVV-21-0173 and the support by the project Advancing University Capacity and Competence in Research, Development, and Innovation ("ACCORD") ITMS2014+: 313021X329, co-financed by resources of the European Regional Development Fund are greatly acknowledged.

## REFERENCES

[1] Tavafoghi, M. et al. 'Silicon-Doped Hydroxyapatite Prepared by a Thermal Technique for Hard Tissue Engineering Applications'. Ceramics International, vol. 44, no. 15. (2018)

[2] Descamps, M. et al. 'Processing and Properties of Biphasic Calcium Phosphates Bioceramics Obtained by Pressureless Sintering and Hot Isostatic Pressing'. Journal of the European Ceramic Society, vol. 33, no. 7, (2013) pp. 1263–70

[3] Dellisanti, F., Valdré, G. 'On the high-temperature structural behaviour of talc (Mg3Si 4O10(OH)2) to 1600C: Effect of mechanical deformation and strain', Philosophical Magazine (2010) pp. 2443–2457

[4] Moreira Mota, L. et al. 'Soapstone reinforced hydroxyapatite coatings for biomedical applications', Surf Coat Technol, vol. 397 (2020)

[5] Lima L. C. B. et al. 'Hybrid Systems Based on Talc and Chitosan for Controlled Drug Release', Materials 2019, vol. 12, no. 21 (2019) pp. 3634

[6] Kumar, P. et al. '3D Printing Technology for Biomedical Practice: A Review'. Journal of Materials Engineering and Performance, vol. 30, no. 7 (2021) pp. 5342–55

# Monitoring of cells collonized hydroxyapatite scaffolds by non-invasive MRI technique

P. Hurik[1], L. Bačiak[2], Z. Varchulová Nováková[3], R. Fialka[1], S. Kašparová[2], M. Janek[1], Ľ. Bača[1]

[1]*Department of Inorganic Materials, FCHPT Slovak University of Technology, Radlinského 9, 812 37 Bratislava, Slovakia*
[2]*Central Laboratories, FCHPT Slovak University of Technology, Radlinského 9, 812 37 Bratislava, Slovakia*
[3]*Comenius University, Faculty of Medicine, Institute of Medical Biology, Genetics and Clinical Genetics, Sasinkova 4, 811 08 Bratislava, Slovakia*

## ABSTRACT

Magnetic resonance imaging (MRI) is a key tool for noninvasive monitoring of living systems with high spatial resolution, especially soft tissues. Whereas computed tomography, which uses ionizing radiation, is the gold standard for monitoring solid tissues. The aim of this study was to prepare a bioceramic scaffold, colonize its surface with mesenchymal stem cells (MSCs) and monitor their activity in situ using MRI. The project involved several steps including testing a suitable filament for 3D printing, subsequent processing of the scaffold by debinding, sintering and incubation of the scaffold with MSCs. Two sets of MRI measurements were performed: one on control scaffolds and the other on scaffolds with cells. From the spatially high-quality MRI-mikroimaging (50μm), we did not detect any stem cell growth on the scaffold at this time point, probably due to the short incubation time. The findings suggest that better results could be achieved with either longer incubation times or *in vivo* MRI experiments using e.g. iron oxide nanoparticles, which could improve the ability to observe new cell growth using MRI.

**Keywords:** hydroxyapatite, 3D printing, scaffolds, MRI, stem cells

## INTRODUCTION

Research into biomaterials has advanced significantly, with a focus on metallic, ceramic, polymeric, 3D printed, and nanomaterials. Hydroxyapatite (HA), a naturally occurring calcium apatite, is crucial for bone tissue engineering due to its exceptional bioactivity, biocompatibility, including osteoconductivity and osteoinductivity[1]. Its structure mimics the mineral component of natural bone, stimulating cell adhesion and proliferation. The field of bone repair is critical, as bone nonunion and delayed healing can lead to a loss of physical independence and a significant socio-economic burden, particularly for the elderly. Modern medicine has driven considerable inventions in this area by introducing new biomaterials, growth factors, and reactive molecules. Current research is exploring novel approaches to improve structural functionality, such as using 3D printing to create patient-specific, personalized scaffolds with microchannels for nutrient delivery.[2] Combined with human medical imaging such as computed tomography (CT) and magnetic resonance imaging (MRI), 3D printing enables for the creation of a variety of bone constructs tailored to the specific damaged areas of a patient. These imaging technologies are also important for monitoring and controlling the tissue regeneration process. While CT is primarily used to image solid tissues, MRI excels at imaging soft tissues and has a key advantage: it is non-invasive and uses a magnetic field instead of harmful ionizing radiation. However, the literature is lacking information on the use of modified bioceramic materials for direct, high-resolution anatomical observation via non-invasive MRI. Researchers are working to enhance the contrast of synthetic bio-ceramics, HA, using labeled materials, including iron oxide nanoparticles, [3,4] for therapeutic

applications. Additionally, their use for direct imaging with high spatial resolution remains an underexplored area.

## EXPERIMENTAL

Samples for MRI measurements were prepared using Creality Ender 5 Pro 3D printer and highly loaded composite filament with 50 wt. % of pharmaceutical-grade HAp powder developed at the Department of Inorganic Materials, STU. This filament was used for production of scaffolds with five different sizes from 5 mm to 30 mm. The printing was done at a nozzle temperature of 200 °C and a bed temperature of 60 °C.

After the debinding procedure at 800 °C for 1h, the samples were sintered at 1300 °C for 1 hour in a high-temperature furnace (CLASIC, Czech Republic). One of the sintered scaffolds was used for the cultivation of the ASTCs. The cells were seeded on a sterilized scaffold at a density of 20,000 cells/scaffold. The presence of cells during the whole process were inspected with an inverted microscope, with one change of the culture medium. The entire culture experiment lasted 6 days, after which the cells on the scaffold were fixed with 4 % paraformaldehyde, which preserved their structure. In this state, the scaffold with the cells was handed over for MRI study.

All MRI experiments were performed on a 4.7 T horizontal magnet (Agilent, Yarnton, UK) equipped with a SGRAD 205/120/HD/S gradient insert with an inner diameter of 12 cm and a maximum gradient intensity of 400 mT/m. A 25 mm diameter quadrature volume RF coil (STARK contrast, Erlangen, Germany) was used to detect the MR signal. FSEMS (fast spin echo multi slice) and GEMS (gradient echo multi slice) 2D sequences with 256x256 pixel resolution with 3 min data acquisition were used to image the scaffold sample in physiologic solution. A FEMS sequence with a resolution of 128x128x128 pixels with a relatively long acquisition time (~9 h 10 min) was used to image the sample in 3D space to achieve isometric resolutions of 0.1 mm and 0.5 mm. A long Repetition Time (TR) of 3000 milliseconds (ms) was used to achieve different contrast characteristics, such as T2-weighting or T1-weighting, depending on the Echo Time (TE).

## RESULTS

All 3D printed samples undergone debinding sequence, where the organic binder was removed from the scaffolds. After removing the binder (**Fig. 1** *left*), the inner walls of the scaffold filler were slightly wavy, which did not pose any problem for the application of stem cells to their surface. After removing the binder, the samples were sintered at 1300 °C for one hour (**Fig. 1** *right*) to achieve the final mechanical properties. For the MRI measurements samples with a diameter of 10 mm were selected, one of which was used for colonization with ATSC cells at the Institute of Medical Biology, Genetics and Clinical Genetics, Faculty of Medicine, UK. The entire cultivation experiment lasted 6 days and after this time the cells on the scaffold were fixed with 4 % paraformaldehyde, which was supposed to preserve their structure. For comparison, the measurement was also performed on a control sample.

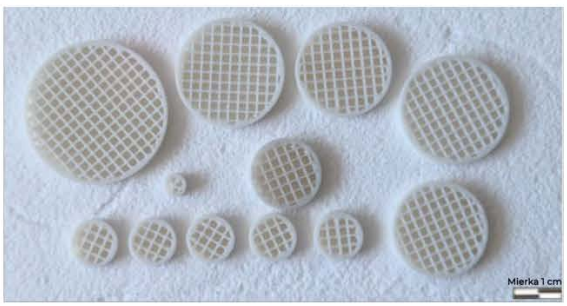


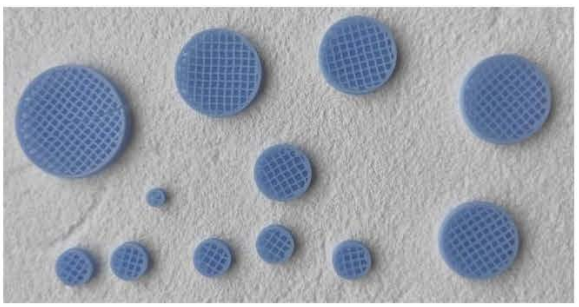

***Fig. 1** HA scaffolds after debinding (left) and after sintering at 1300 °C / 1h (right)*

The results of MRI measurements showed (**Fig. 2**) that despite the relatively high-quality MRI imaging of the prepared samples, the MRI method did not revealed the changes in HA simulated bone tissue by the adhered cells after the colonization time of 6 days used. Unfortunately, no difference was observed on the samples, which indicates that a) MRI resolution is insufficient to visualize cells present; b) the surface cell population was possibly too thin to observe changes; or c) ATSC cells did not attach effectively to the surface of the bioceramic scaffold used.

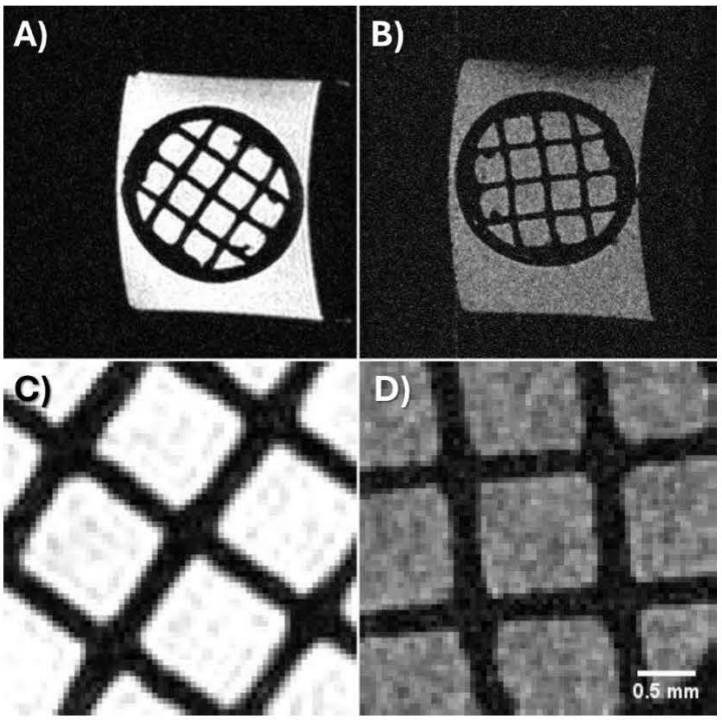


***Fig. 2** HA scaffold measured using a spin echo 3D sequence with isometric resolution of 0.1 mm (A) and 0.05 mm (B). Lower 4x zoom of the same slice (C, D). Image (D) without interpolation, only with the use of a time domain weighting filter for noise suppression*

It seems that the current limitations of MRI technology would allow mostly long-term observations of regeneration with greater bone tissue increment or remodeling. However, there can be found notice in the literature about the insufficient ability of human ATSCs to form ectopic bone compared to BMSCs. In this study, the adipose-derived stem cells (ATSCs) were chosen because of their availability. ATSCs are more abundant, easier to harvest with higher yields, and have faster proliferation rates, making them a favorable source for clinical applications where a large cell number is required. On the other hand, the BMSCs generally show superior osteogenic capacity, displaying greater alkaline phosphatase (ALP) activity and calcium deposition compared to ASCs. However, the isolation of BMSCs from bone marrow aspirates involves a more invasive procedure, leading to lower cell yields and increased patient discomfort. Brocher et. al speculated that insufficient ability of human ATSCs to form ectopic bone compared to BMSCs could be due to reduced osteogenic cell commitment (lower expression of BMP-2 and BMP-4), lower proangiogenic activity (less VEGF, angiopoietin and IL-6) and/or increased production of hormones expressed in adipose tissue, such as visfatin. They suggest that multiclonal populations of ATSCs from liposuction material should therefore not be considered skeletal stem cells, as they are not capable of initiating a new bone organ growth without additional factors, inducing a skeletogenic transcriptional program.[5] When

comparing 2D and 3D images, less pronounced artifacts in 3D images were observed, which are caused by the possibility of spatial alignment of the section plane to the level of the sample plane. Subsequently, by evaluating line profile or thresholding a smaller measurement error could be achieved. Thanks to this, the sequence is less sensitive to the mismatch between the section planes and the sample plane. When setting the MRI to microimaging, long-term accumulation of the MR signal (about 9 hours) resulted in a resolution of 0.05 mm, which is 50 μm, which theoretically could be sufficient for continuous monitoring of bone tissue growth. The literature states that the size of MSC cells is 10–30 μm[6], however, the size and shape may vary depending on the source. For example, ATSC cells from male Wistar rats varied in shape and size from small wavy cells to larger oval cells.[7] If the size of ATSC cells were at the resolution of MRI, it is highly likely that bone growth or cell activity would be visible, as the commonly used MRI resolution in this work was 0.1 mm and the slice thickness 0.5 mm. These results represent an initial study of the use of MRI analysis for the possible imaging of cells, closely surrounded or firmly attached to a hydroxyapatite scaffold. Considering the sensitivity of MRI imaging, several strategies for enhancing detection sensitivity can be explored e.g. by applying longer cultivation time and/or the labelling of stem cells e.g. with iron-based nanoparticles. The labeling approach would help in detecting attached stem cells, especially in case the cells did not proliferate enough into hard bone tissue to gain intrinsic contrast compared to saline.

## CONCLUSIONS

In this study, hydroxyapatite scaffolds of various sizes were successfully fabricated using filament 3D printing. The scaffolds were seeded with adipose-derived stem cells (ATSCs) for six days and subsequently imaged using micro-MRI (μMRI) to assess colonization. Our analysis compared spin-echo and gradient-echo sequences and found slight disadvantages of the gradient-echo method. Despite high-resolution imaging (50 μm isotropic resolution), no significant differences were detected between cell-seeded scaffolds and control scaffolds using μMRI. This study provides a basis for evaluating the capabilities of μMRI to image small samples and suggests the potential for using MRI for repeated measurements of implanted bioceramic scaffolds in vivo.

## ACKNOWLEDGMENT

The financial support of the Slovak Grant Agency VEGA (grant number VEGA 1/0070/22) and the Agency for Research and Development Support under contract No APVV-21-0173 and the support of the project Increasing the Capacities and Competences of Universities in Research, Development and Innovation ("ACCORD") ITMS2014+:313021X329, co-funded by the European Regional Development Fund, is gratefully acknowledged.

## REFERENCES

[1] Kang HJ, Makkar P, Padalhin AR, Lee GH, Im SB, Lee BT. Comparative study on biodegradation and biocompatibility of multichannel calcium phosphate based bone substitutes. *Materials Science and Engineering: C*. 2020;110:110694. doi:10.1016/j.msec.2020.110694

[2] Gaharwar AK, Mihaila SM, Swami A, et al. Bioactive Silicate Nanoplatelets for Osteogenic Differentiation of Human Mesenchymal Stem Cells. *Advanced Materials*. 2013;25(24):3329-3336. doi:10.1002/adma.201300584

[3] Mushtaq A, Tang Z, Hou Y, et al. Biocompatible magnetic hydroxyapatite $Fe_3O_4$-HAp nanocomposites for T1-magnetic resonance imaging guided photothermal therapy of breast cancer. *Mater Today Commun.* 2022;31:103734. doi:10.1016/j.mtcomm.2022.103734

[4] Sun L, Li X, Wei X, et al. Stimuli-Responsive Biodegradable Hyperbranched Polymer–Gadolinium Conjugates as Efficient and Biocompatible Nanoscale Magnetic Resonance Imaging Contrast Agents. *ACS Appl Mater Interfaces.* 2016;8(16):10499-10512. doi:10.1021/acsami.6b00980

[5] Brocher J, Janicki P, Voltz P, et al. Inferior ectopic bone formation of mesenchymal stromal cells from adipose tissue compared to bone marrow: Rescue by chondrogenic pre-induction. *Stem Cell Res.* 2013;11(3):1393-1406. doi:10.1016/j.scr.2013.07.008

[6] Moll G, Le Blanc K. Engineering more efficient multipotent mesenchymal stromal (stem) cells for systemic delivery as cellular therapy. ISBT Sci Ser. 2015;10(S1):357-365. doi:10.1111/voxs.12133

[7] Feretis T, Katselis C, Papanikolaou IG, et al. Original Article ATSC Transplantation Contributes to Liver Regeneration Following Paracetamol-Induced Acute Liver Injury through Differentiation into Hepatic-like Cells. http://www.vergeriomangimi.it/

# Stoichiometry and transition metal type effects in the compositionally complex (TiZrHf-V/Nb/Ta)$_{100-z}$-N$_z$ coatings: A review

F. Lofaj*[1], L. Kvetková[1], P. Hviščová[1], T. Roch[2], T. Fiantok[2], D. Albov[1], M. Mikula[2]

[1]*Institute of Materials Research of the Slovak Academy of Sciences, Slovakia*
[2]*Faculty of Mathematics, Physics and Informatics, Comenius University in Bratislava, Slovakia*

## ABSTRACT

Among the family of compositionally complex nitride (CCN) PVD coatings, the systems based on transition metals (TM) from the 4$^{th}$ and 5$^{th}$ group of elements exhibit attractive mechanical properties. The aim of the current work is to review the influence of the additions of Ta, Nb and V into (TiHfZr)-N matrix during reactive sputtering on their structure and mechanical properties to determine the effects of individual TMs and nitrogen stoichiometry. The reviewed coatings were deposited using reactive DC magnetron sputtering (rDCMS) and reactive High Target Utilization Sputtering (rHiTUS) in hysteresis-free regime. The highest hardness and indentation moduli were observed in TiZrHf-N coatings with near-stoichiometric compositions. The additions of V, Nb and/or Ta slightly reduced the corresponding values, i.e. synergy effect was negative. Despite that, the work confirms the ability of reactive HiTUS to produce multicomponent high entropy nitrides with mechanical properties similar to those from reactive DC magnetron sputtering.

**Keywords:** high entropy nitride coatings, compositionally complex nitrides, reactive sputtering, refractory metal additions, stoichiometry

## INTRODUCTION

The transition from binary and ternary compounds toward multi-element systems pioneered by the bulk and coating "high entropy alloys" (HEA) [1-2] and ceramics [3-4] is one of the ways to achieve better mechanical and functional properties. In the case of PVD multi-TM nitride coatings, hardness values in from 8 GPa to 51 GPa and their indentation moduli from 267 GPa up to 500 GPa were found [5-9]. Moreover, their thermal stability exceeded 1200°C [10] and they exhibited improved corrosion resistance [11] and even biocompatibility [8]. The earlier theoretical predictions to form single phase solid solutions in 5 transition metal-carbide systems based on valence electron concentration (VEC) and entropy-forming ability (EFA) favored TiZrHf-NbTa, TiHf-VNbTa and TiZr-VNbTa combinations [12]. More sophisticated disordered enthalpy-entropy descriptor (DEED) [13] predicted synthesizability of (bulk) stoichiometric equimolar carbide, carbonitride, and even boride systems The DEED based predictions agreed better with the experimental data. Interestingly, the 6RM-carbides and carbonitrides were ranked lower than any 5RM-C(N) and the highest synthesizability exhibited TiZrHf-CN system. Despite DEED values for the analogous nitrides were not calculated, the extrapolation from carbide and carbonitride data suggests that the refractory metals from group IV and V should also form disordered homogeneous nitride solid solutions. It is further supported by the facts that all these metals were classified as strong nitride formers [14] and most of the 5TM- and 6TM-nitride coatings were already prepared experimentally. The above results imply that V, Nb and Ta might have different influence not only on bulk synthesizability but also on coating characteristics. However, only limited information on the effects of individual refractory metals in the multi-RM-nitrides is available up to now. Therefore, the aim of the current work was to investigate the effects of refractory Ta, Nb, and V added into the reference (TiHfZr)-N$_z$ coatings deposited by r-DCMS and r-HiTUS on their structure and

mechanical properties to estimate their potential for highly demanding applications at high- and ultra-high temperatures.

## EXPERIMENTAL

Four reactive DCMS and four rHiTUS coating series were deposited on the polished (0001) sapphire and (111) Si wafer substrates using a balanced DC magnetron sputtering (model Cryofox 500, Polyteknik, Denmark) and HiTUS (model S500, Plasma Quest Ltd., UK) deposition system, respectively. The series differed by the composition of the 3TM+ME (ME = -, V, Nb, Ta) targets while keeping the same deposition conditions. The composition of the target slightly varied around equimolar composition whereas the concentrations to compensate for the differences in the sputter yields of different TMs. The deposition procedures followed the steps and conditions optimized in our earlier studies deposition in both case [15-16]. Note that the reactive processes occurred in hysteresis-free regime due to high pumping speeds in both cases [17]. The main variable in each series was the flow of nitrogen $x$ (in sccm), added into the Ar atmosphere.

The structure and composition of the studied coatings were observed using scanning electron microscopy (SEM) (models FESEM/FIB Auriga Compact and EVO MA 15, Zeiss, Germany). The average chemical compositions of the coatings were determined using energy dispersive spectroscopy (EDS), and a combination of several Ion Beam Analysis (IBA) methods on a 6 MV tandem ion accelerator (Tandetron, HVE, Groningen, The Netherlands) [18] including Rutherford and Elastic (non-Rutherford) Backscattering Spectrometry (RBS/EBS) and Nuclear Reaction Analysis (NRA). The phase composition of the coatings was determined using X-ray diffraction (Rigaku Ultima IV) with parallel beam $CoK_{\alpha}$ radiation in symmetrical and grazing incidence (GI) configurations. Mechanical properties of the coatings were measured by instrumented indentation (model G 200, Agilent, USA) using the continuous stiffness method for thin films (CSMTF) [19] up to 500 nm depths.

## RESULTS

SEM observation of the cross sections after fracture revealed that the coating thicknesses decreased from around 830 nm at 0 sccm $N_2$ to 480 nm at 10 sccm $N_2$. **Fig. 1** summarizes the changes in coating composition obtained by EDS with the increase of nitrogen flow in the studied rDCMS and rHiTUS TiZrHf-ME-xN systems. All dependences exhibit similar behavior: nitrogen concentrations increased approximately linearly proportionally to the nitrogen flow until saturation at critical flows varying around 5 sccm $N_2$. The normalization of the concentrations to 100 % caused that nitrogen the increase of nitrogen concentration decreased the concentrations of TMs. Despite equiatomic concentrations of the metals in the composite target, the concentrations of Ti were always the highest, those of Hf the lowest. These deviations were attributed to different sputtering yields and caused that the studied coatings can be classified as the „compositionally complex“, or „complex concentrated“ nitrides which form wider family than the ideal equimolar „high entropy stabilized“ nitrides [20-21].

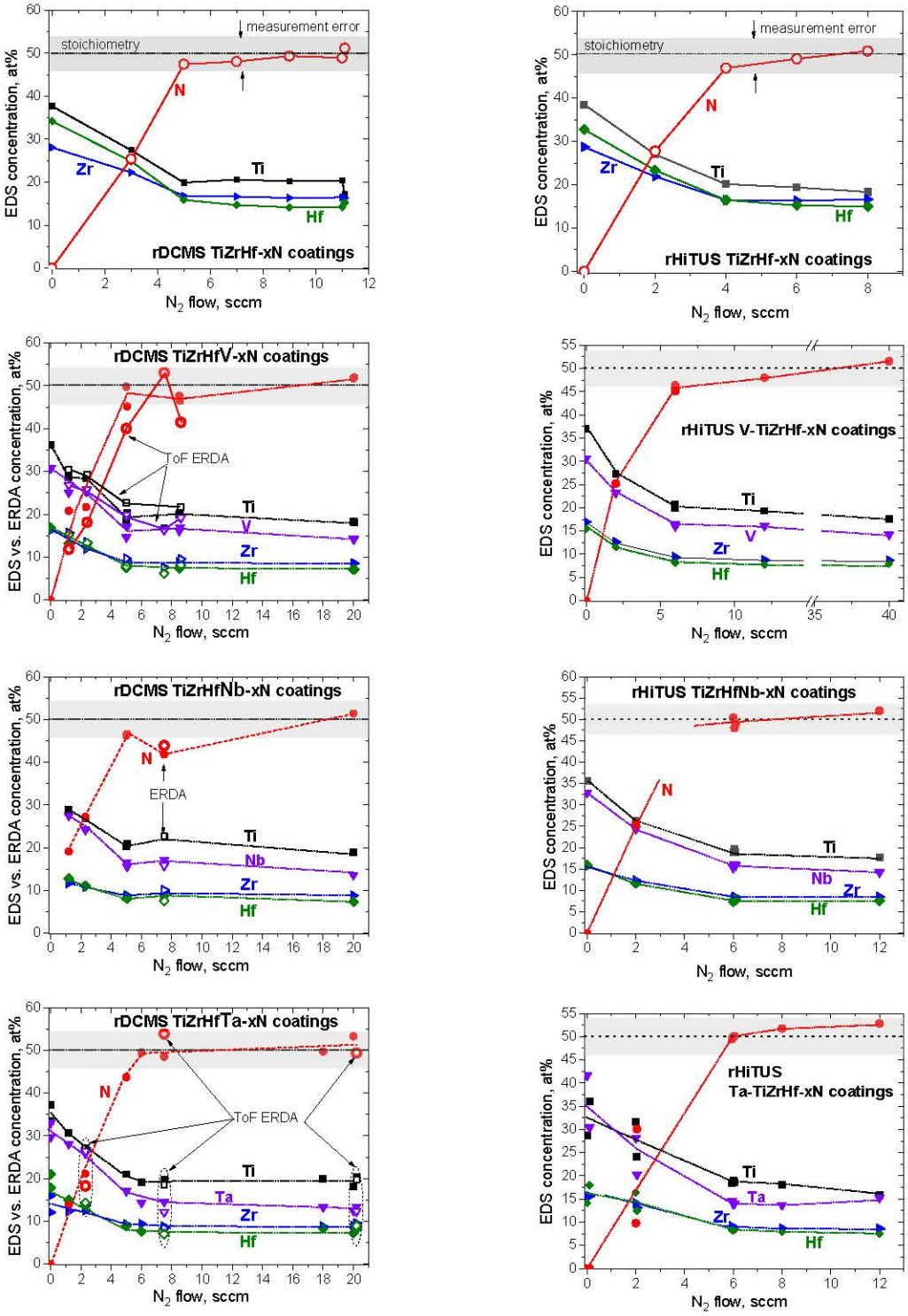


***Fig. 1*** *The evolutions of the EDS average concentrations of nitrogen and refractory metals in ME-TiZrHf-xN coatings (ME = -, V Nb, and Ta) depending on nitrogen flow, x, deposited by reactive DCMS and reactive HiTUS. In Figures "ToF ERDA" stand for Time-of-flight Elastic Recoil Detection Analysis*

Analogous results from TiZrHfVNbTa-N coatings suggest that a transition from metallic via sub/stoichiometric nitride up to stoichiometric nitride occurs during linear concentration increase and the saturation corresponds to the stoichiometric composition. Such explanation is a basis for the vacancy occupancy model assuming gradual occupancy of the octahedral sites

in the cubic metallic structure (usually bcc) by nitrogen, and after critical nitrogen concentration is achieved, transformation into fcc and occupancy of the vacancies in non-metallic (nitrogen) sub-lattice until its saturation [10, 15-16]. Such explanation is in consent with the dependences of the mechanical properties. **Fig. 2** summarizes the results of nanoindentation tests.

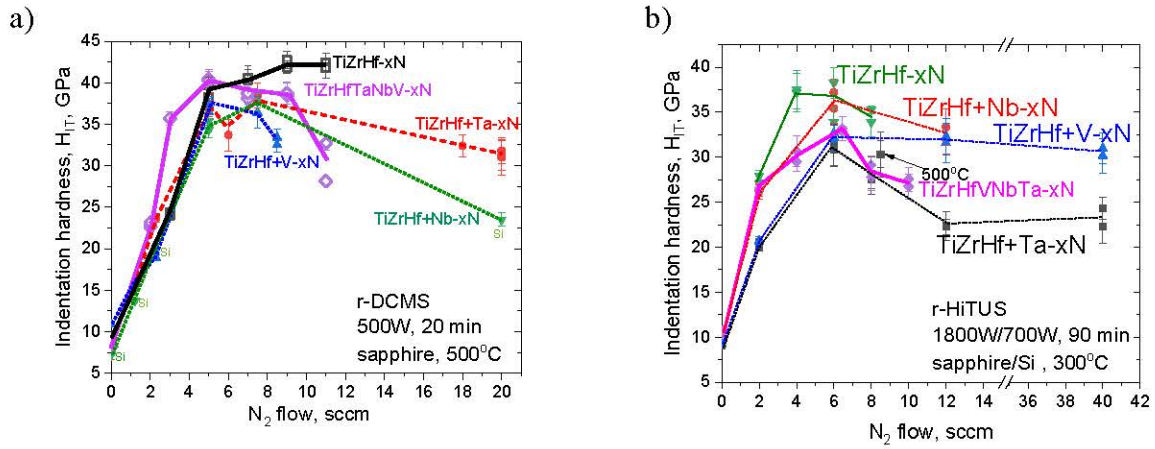


***Fig. 2*** *Hardness dependences of the studied TiZrHf-ME-xN coatings produced by a) – r-DCMS and b) - r-HiTUS, as a function of nitrogen flow, x*

The hardness rapidly increased up to a maximum of 32-37 GPa at $x$ = 5 sccm in r-DCMS and to 31-37 GPa at 6 sccm in r-HiTUS. At higher flows, small degradation was observed in all cases. In comparison to the behavior of TiZrHf-xN the addition of the fourth transition metal slightly (around 10 %) reduced the obtained hardness values. Thus, the synergy effect from the additional TM elements into TiZrHf-sublattice was not observed. Despite that, the work confirms the ability of reactive HiTUS to produce multicomponent high entropy nitrides with mechanical properties similar to those from reactive DC magnetron sputtering.

## CONCLUSIONS

The additions of V, Nb and/or Ta into TiZrHf-N system generate homogeneous solid solutions with slightly reduced hardness, i.e. synergy effect expected in HEN was not confirmed.

## ACKNOWLEDGMENT

This work was supported by the **EU** NextGenerationEU through the Recovery and Resilience Plan for Slovakia under project No. 09I03-03-V04-00281 and by the Slovak Research and Development Agency (projects APVV 21-0042 and APVV-24-0038).

## REFERENCES

[1] B. Cantor, I.T.H. Chang, P. Knight, A.J.B. Vincent, Microstructural development in equiatomic multicomponent alloys, Mater. Sci. Eng. A 375-377 (2004) 213-218. https://doi.org/10.1016/j.msea.2003.10.257

[2] J.-W. Yeh, S.-K. Chen, S.-J. Lin, J.-Y. Gan, T.-S. Chin, T.-T. Shun, C.-H. Tsau, S.-Y. Chang, Nanostructured high-entropy alloys with multiple principal elements: Novel alloy design concepts and outcomes, Adv. Eng. Mater. 6 (2004) 299-303. https://doi.org/10.1002/adem.200300567

[3] R.Z. Zhang, M.J. Reece, Review of high entropy ceramics: Design, synthesis, structure and properties, J. Mater. Chem. A, 7 (2019) 22148-22162. https://doi.org/10.1039/c9ta05698j

[4] A.J. Wright, J. Luo je neskor] [C. Oses, C. Toher, S. Curtarolo, High entropy ceramics. Nat. Rev. Mater., 5 (2020) 295-309. https://doi.org/10.1038/s41578-019-0170-8

[5] S.-C. Liang, Z.-C. Chang, D.-C. Tsai, Y.-C. Lin, H.-S. Sung, M.-J. Deng, F.-S. Shieu, Structural and mechanical properties of multi-element (TiVCrZrHf)N coatings by reactive magnetron sputtering, Appl. Surf. Sci. 258 (2011) 399-403. https://doi.org/10.1016/j.apsusc.2011.09.006

[6] O.V. Sobol, A.A. Andreev, V.F. Gorban, N.A. Krapivka, V.A. Stolbovoi, I.V. Serdyuk, and V.E. Fil'chikov, Reproducibility of the single-phase structural state of the multielement high-entropy Ti–V–Zr–Nb–Hf system and related superhard nitrides formed by the vacuum-arc method, Techn. Physics Lett. 38 (2012) 40–47. https://doi.org/10.1134/S1063785012070127

[7] A.D. Pogrebnjak, I.V. Yakushchenko, G. Abadias, P. Chartier, O.V. Bondar, V.M. Beresnev, Y. Takeda, O.V. Sabol', K. Oyiosji, A.A. Andreyev, B.A. Mukushev, The effects of the deposition parameters of nitrides of high-entropy alloys (TiZrHfVNb)N on their structure, composition, mechanical and tribological properties, J. Superhard Mater. 35 (2013) 356-368. https://doi.org/10.3103/S106345761306004X

[8] V. Braic, M. Balaceanu, M. Braic, A. Vladescu, S. Panseri, A. Russo, Characterization of multi-principal-element (TiZrNbHfTa)N and (TiZrNbHfTa)C coatings for biomedical applications, J Mech. Behav. Biomed. Mat. 10 (2012) 198-205. https://doi.org/10.1016/j.jmbbm.2012.02.020

[9] V. Braic, A. Vladescu, M. Balaceanu, C.R. Luculescu, M. Braic, Nanostructured multi-element (TiZrNbHfTa)N and (TiZrNbHfTa)C hard coatings, Surf. Coat. Technol. 211 (2012) 117-121. https://doi.org/10.1016/j.surfcoat.2011.09.033

[10] A. Kirnbauer, A. Kretschmer, C.M. Koller, T. Wojcik, V. Paneta, M. Hans, J.M. Schneider, P. Plocik, P.H. Mayrhofer, Mechanical properties and thermal stability of reactively sputtered multi-principal-metal Hf-Ta-Ti-V-Zr nitrides, Surf. Coat. Technol. 389 (2020) 125674. https://doi.org/10.1016/j.surfcoat.2020.12

[11] S.K. Bachani, C.-J. Wang, B.-S. Lou, L.-C. Chang, J.-W. Lee, Fabrication of TiZrNbTaFeN high-entropy alloys coatings by HiPIMS: Effect of nitrogen flow rate on the microstructural development, mechanical and tribological performance, electrical properties and corrosion characteristics, J. Alloys Compounds. 873 (2021) e159605. https://doi.org/10.1016/j.jallcom.2021.159605

[12] P. Sarker, T. Harrington, C. Toher, C. Oses,M. Samiee, J.-P. Maria, D.W. Brenner, K.S. Vecchio,S. Curtarolo, High-entropy high-hardness metal carbides discovered by entropy descriptors, Nat Commun. 9 (2018) 4980. https://doi.org/10.1038/s41467-018-07160-7

[13] S. Divilov, H. Eckert, D. Hicks, C. Oses, C. Toher, et.al., Disordered enthalpy-entropy descriptor for high-entropy ceramics discovery, Nature 625 (2024) 66-73. https://doi.org/10.1038/s41586-023-06786-y

[14] E. Lewin, Multi-component and high-entropy nitride coatings - A promising field in need of a novel approach, J. Appl. Phys. 127 (2020) e160901. https://doi.org/10.1063/1.5144154

[15] F. Lofaj, P. Hviščová, T. Roch, V.Girman, M. Kabátová, J. Dobrovodský, Hysteresis-free reactive DC magnetron sputtered TiZrHfVNbTa-xN coatings: Structure and mechanical properties, Int. J. Refrac. Met. Hard Mater., 128 (2025) 107024. https://doi.org/10.1016/j.ijrmhm.2024.107024

[16] F. Lofaj, L. Kvetková, T. Roch, J. Dobrovodský, V. Girman, M. Kabátová, M. Beňo, Reactive HiTUS TiNbVTaZrHf-$N_x$ Coatings: Structure, Composition and Mechanical Properties, Materials 16 (2023) 563. https://doi.org/10.3390/ma16020563

[17] F. Lofaj, M. Fekete, L. Kvetková, P. Hviščová, O. Petruš, Understanding hysteresis-free reactive DC magnetron and High Target Utilization sputtering of TiZrHfVNbTa-N coatings, Int. J. Adv. Ceram. Technol. (2025) e70087. https://doi.org/10.1111/ijac.70087

[18] J. Dobrovodský, M. Beňo, D. Vaňa, P. Bezák, P. Noga, The first year operation experience with Ion Beam Analysis at the new STU Ion Beam Laboratory. Nucl. Instrum. Methods Phys. Res. Sect. B Beam Interact. Mater. Atoms., 450 (2019) 168–172. https://doi.org/10.1016/j.nimb.2018.10.006

[19] J. Hay, B. Crawford, Measuring substrate independent modulus of thin films, J. Mater. Res. 26 (2011) 727-738. https://doi.org/10.1557/jmr.2011.8

[20] S. Gorsse, J.-P. Couzinié, D.B. Miracle, From high-entropy alloys to complex concentrated alloys, Comptes Rendus Physique, 19 (2018) 21-736. https://doi.org/10.1016/j.crhy.2018.09.004

[21] A.J. Wright, J. Luo, A step forward from high-entropy ceramics to compositionally complex ceramics: a new perspective, J. Mater. Sci., 55 (2020) 9812-9827. https://doi.org/10.1007/s10853-020-04583-w

# Mechanical properties of SiC/NbC ceramic composites: Comparison of conventional and reactive processing methods

R. Sedlák[1*], M. Hrubovčáková[1], L. Ďaková[1], I. Shepa[1], A. Kovalčíková[1], P. Hviščová[1], O. Petruš[1], T. Csanádi[1]

[1]*Institute of Materials Research, Slovak Academy of Sciences, Division of Ceramic and Non-Metallic Systems, Watsonova 47, 040 01 Košice, Slovak Republic*

## ABSTRACT

In this study, SiC/NbC composites were fabricated by spark plasma sintering (SPS) using two distinct approaches: conventional powder consolidation (samples labelled $SiC_C$) and *partially reactive processing* via in-situ SiC formation (samples labelled $SiC_R$). NbC was introduced as a secondary phase in amounts of 5, 10, and 20 wt. % in the form of fine particles. The resulting composites were systematically examined in terms of microstructure, phase composition, and mechanical performance. Mechanical testing revealed that composites produced by reactive processing exhibited slight improvement in hardness and fracture toughness, which are attributed to strong SiC–NbC chemical interactions and refined microstructural features. Particular attention was given to the chemical incorporation of NbC particles into the SiC matrix, a crucial step toward the future reinforcement of the in-situ-grown SiC ceramic matrix, with interconnected, interwoven bonds of NbC fibers.

**Keywords:** carbides; ceramic composite materials; sintering; silicon carbide; niobium carbide

## INTRODUCTION

Silicon carbide (SiC) and niobium carbide (NbC) are advanced ceramic materials characterised by outstanding hardness, thermal stability, and chemical resistance, making them suitable for applications in extreme environments. Despite its potential as a ceramic matrix material, the intrinsic brittleness of SiC restricts its broader implementation, highlighting the need for strategies to enhance its fracture toughness [1-4]. Improvement of the mechanical and functional properties of SiC is often achieved by forming composite systems through the addition of a secondary phase. NbC is an attractive reinforcing component due to its high melting point (around 3600 °C), excellent chemical stability and good compatibility with SiC. The presence of NbC can contribute to the suppression of grain growth during sintering, increasing the hardness, strength and improving the thermal stability of the composite. In addition, NbC can influence the microstructural development during sintering processes, such as SPS, thus allowing high density to be achieved at relatively low temperatures [5]. In recent years, there has been increasing interest in the research of SiC–NbC composites, which combine the advantages of both carbides and represent a promising class of ultra-high temperature (UHTC) materials. Despite several works focused on the micromechanical behaviour or oxidative stability of similar systems, the mechanism of interactions between SiC and NbC during sintering, as well as their influence on the resulting microstructure and properties, remains insufficiently understood [6-8]. The aim of this work is therefore to study the influence of NbC addition on the microstructural development, density and mechanical properties of SiC-based ceramic composites prepared by SPS. The knowledge gained may contribute to the optimisation of the processing and design of new high-performance carbide materials intended for extreme thermal and mechanical conditions.

## EXPERIMENTAL

Composites based on SiC (Beta-Silicon Carbide SiC GRADE BF 17, H.C. STARCK), with varying amounts of 5, 10, and 20 wt. % of NbC (Niobium carbide, 99+ % (metals basis), <10 Micron Powder, Thermo Scientific Chemicals) were prepared from commercially available powders. The average particle size of initial SiC was 0.50 µm, and for NbC, it was less than 10 µm. Sintering of SiC requires the usage of some sintering additives in these experiments, 0.3 wt. % of B (Boron powder, Merck) and 1 wt. % of C (Carbon black, Super P Conductive; 99 % (metals basis), abcr). The powders were milled in a planetary ball mill (Retsch PM 200) at 250 rpm for 4 h in a WC jar, using Isopropanol as a solvent. WC balls (10 mm) were used as the milling medium, with a powder-to-ball weight ratio of 1:10. The prepared powder mixture was placed into a graphite die (20 mm) and consolidated via SPS (model HP D10-SD, FCT Systeme). Two sets of reference materials and composites with NbC were prepared. One by the conventional method (samples labelled $SiC_C$) and the other reactive approach (samples labelled $SiC_R$) by adding 5 wt. % Si (Silicon powder, crystalline, -325 mesh, 99.5 % (metals basis), Thermo Scientific Chemicals) and 5 wt. % C (Carbon black, Super P Conductive; 99 % (metals basis), abcr) for the creation of in-situ SiC and for better incorporation of NbC into the matrix. The sintering parameters were: heating up 100 °C/min; 2100 °C/10 min hold; 100 °C/min cooling; in vacuum at a pressure of 70 MPa. The density of the samples was measured by the Archimedes method in distilled water. Specimens for microstructure observation and mechanical investigation were prepared by a routine ceramographic procedure. They were cut, ground, and polished to a 0.1 µm finish. The microstructural characterisation was determined by SEM (FIB-SEM ZEISS AURIGA Compact). Hardness was determined by Vickers indentation at 1 kg and 10 kg (Wolpert Wilson 432 SVD Vickers Hardness Tester). The indentation toughness was calculated from the Anstis equation, and the elastic modulus was measured by the resonant frequency method (Buzz-o-sonic Lab Kit 5.9 by BuzzMac International, LLC).

## RESULTS

The presented **Fig. 1** illustrates the key parameters of the thermomechanical cycle during the conventional sintering of a powder mixture of $SiC_C$ with 10 % NbC using the SPS method. The experiment was characterised by phases of rapid temperature increase, isothermal dwell, and controlled cooling under applied pressure. The initial heating phase proceeded with a controlled temperature ramp-up rate, leading to the attainment of the maximum sintering temperature of 2100 °C (red curve). Concurrently, pressure was applied (blue curve), which increased from an initial value to 70 MPa. This combination of high temperature and pressure drove the material densification.

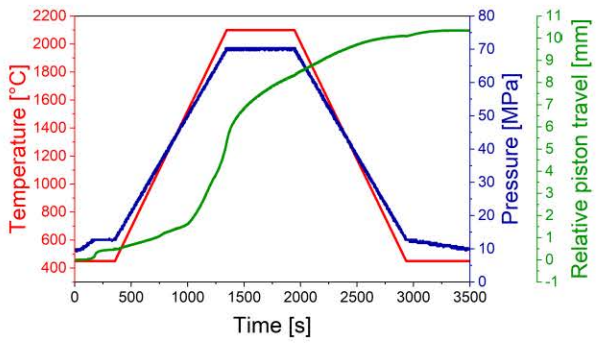


***Fig. 1*** *Schematic illustration of individual SPS sintering steps for material $SiC_C$-10NbC*

The curve representing the relative piston travel (green curve) serves as a direct indicator of sample densification; the primary increase in piston displacement (from approximately 0 mm to 9 mm) occurred during the high-temperature phase of the heating cycle (1200 °C – 2000 °C), where intensive material flow and pore elimination took place. After reaching 2100 °C, the sample was maintained in the isothermal phase under constant pressure, which led to the completion of densification, with the total piston travel reaching a maximum of 10.5 mm. The dwell phase was followed by rapid cooling, during which the mechanical load remained preserved, and its release occurred only at a relatively low temperature.

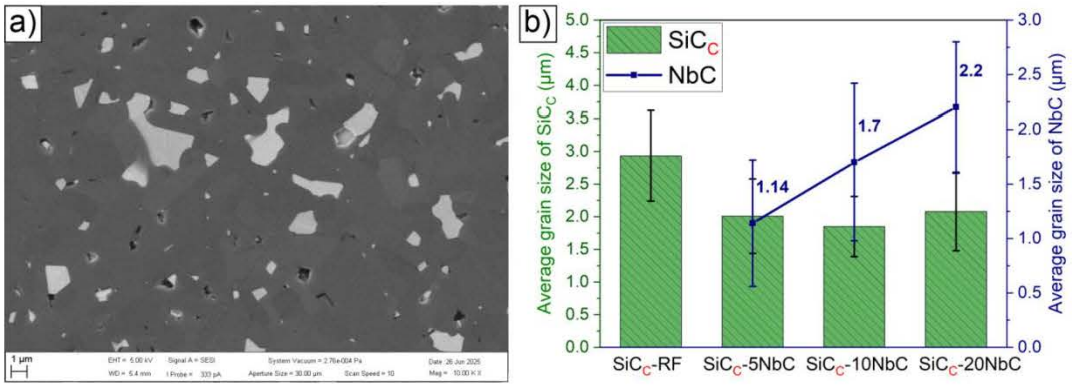


***Fig. 2*** *a) Microstructure of the SiCC-10NbC composite; b) Effect of NbC addition on the average grain size of SiCC composites*

The SEM micrograph **Fig. 2a)** reveals a fine-grained, dual-phase microstructure of the $SiC_C$–10 % NbC composite, sintered by the SPS method. The darker-grey phase represents the SiC matrix, while the brighter-grey phase is the dispersed NbC particles. Morphologically, the NbC primarily concentrates as an intergranular phase, effectively acting as a grain growth inhibitor for the $SiC_C$ matrix. The presence of these dispersed NbC particles inhibits the migration of $SiC_C$ grain boundaries during the high-temperature isothermal sintering stage. Quantitative grain size analysis, conducted using the ImageJ software, is illustrated in the accompanying plot **Fig. 2b)** and confirms this inhibitory mechanism: while pure $SiC_C$ achieved an average grain size of approximately 3.5 μm, samples with the NbC addition exhibited a reduction in grain size to approximately 1.8 μm. This refinement effect is crucial for optimising the material's mechanical performance.

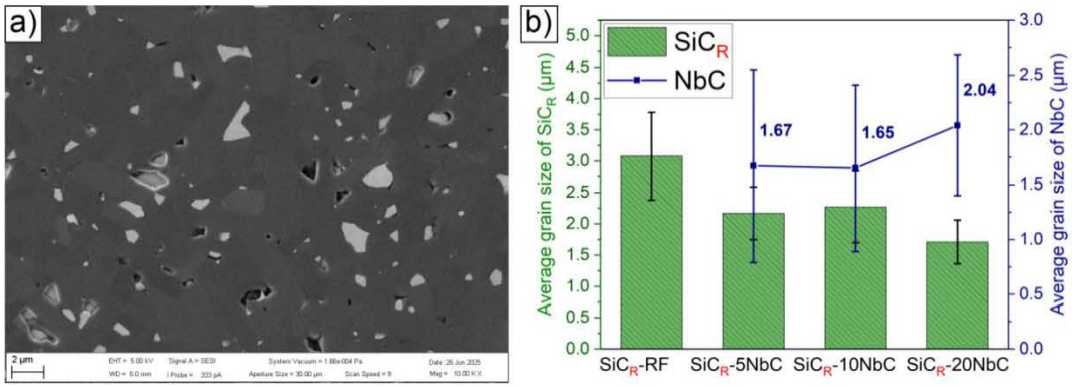


***Fig. 3*** *a) Microstructure of the $SiC_R$-10NbC composite; b) Effect of NbC addition on the average grain size of $SiC_R$ composites*

The presented SEM micrograph of the dual-phase microstructure of the $SiC_R$–10 % NbC composite **Fig. 3a)**, sintered by the SPS method, confirms the presence of a darker-grey SiC matrix and a lighter-grey dispersed NbC phase. The key difference compared to the previous material prepared by conventional sintering from commercial powder ($SiC_C$) lies in the

preparation process (reaction synthesis). Grain size analysis **Fig. 3b)** shows that the $SiC_R$–10 % NbC composite achieved a higher average grain size of 2.2 μm. This lower slowing-down efficiency suggests that the energetic and rapid reaction mechanisms associated with the in-situ formation of SiC led to a stronger, localised tendency for grain growth. This strong growth partially overcame the inhibitory effect of NbC, resulting in a final microstructure that is finer than pure SiC without additives, but possesses a larger average grain size than the composite prepared from the commercial, finer starting SiC powder.

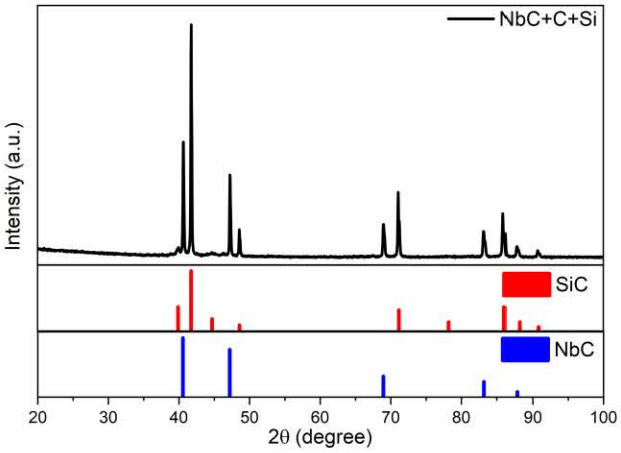


***Fig. 4*** *XRD phase composition of $SiC_R$-10NbC composite*

The measurements were performed (Philips X'Pert Pro, Malvern Panalytical) in Bragg–Brentano geometry. Measured data were evaluated by (High Score, Malvern Panalytical) using the PDF-2 database for identification of the individual phases. From the acquired data in Figure 4, it can be concluded that the partial reaction sintering was complete and the elements Si and C were able to be incorporated into the formation of the SiC (PDF–00-038-1364) matrix with the addition of the NbC (PDF–00-022-1273) secondary phase.

Summary results of basic mechanical properties are given in the tables for materials prepared by the conventional processing approach in **Table 1** and for materials prepared by a partially reactive method in **Table 2**. According to the measured values is evident that the reactive SPS route is a more effective method of preparation in terms of better compaction of materials. Almost fully dense materials were achieved up to the addition of 20 wt. % of NbC. Better compacting process also reflects in the increased values of hardness and indentation fracture toughness (verification through standardised SEVNB method for $K_{IC}$ is needed).

***Table 1*** *Table of properties for materials fabricated by a conventional processing approach*

| Sample name | Relative density (%) | Hardness HV1 (GPa) | Indentation fracture toughness / Anstis HV10 ($MPa.m^{1/2}$) | Elasitc modulus (GPa) |
|---|---|---|---|---|
| $SiC_C$-RF | 99.90 | 28.95 ± 1.21 | 1.63 ± 0.11 | 453.26 |
| $SiC_C$-5NbC | 95.44 | 29.56 ± 1.23 | 1.92 ± 0.16 | 438.36 |
| $SiC_C$-10NbC | 93.20 | 28.95 ± 1.56 | 1.90 ± 0.05 | 445.42 |
| $SiC_C$-20NbC | 88.86 | 27.98 ± 0.88 | 2.19 ± 0.06 | 462.36 |

***Table 2*** *Table of properties for materials fabricated by a partially reactive processing approach*

| Sample name | Relative density (%) | Hardness HV1 (GPa) | Indentation fracture toughness / Anstis HV10 ($MPa.m^{1/2}$) | Elasitc modulus (GPa) |
|---|---|---|---|---|
| $SiC_R$-RF | 99.98 | 30.65 ± 2.09 | 2.69 ± 0.06 | 453.03 |
| $SiC_R$-5NbC | 99.80 | 28.37 ± 0.47 | 2.81 ± 0.05 | 437.90 |
| $SiC_R$-10NbC | 98.45 | 29.68 ± 1.49 | 2.92 ± 0.07 | 449.00 |
| $SiC_R$-20NbC | 93.70 | 29.13 ± 1.68 | 3.07 ± 0.07 | 455.90 |

A more fundamental influence of a conventional or reactive approach on the results of elastic properties was not observed. These partial results will be confronted with reaction-prepared composites reinforced with NbC fibers in the next phase of the study.

## CONCLUSIONS

Microstructural analysis by SEM confirmed the uniform dispersion of NbC particles in the SiC matrix, with significant differences in interfacial bonding depending on the processing method. Mechanical characterisation revealed a slight improvement in hardness and indentation fracture toughness of the composites obtained by reactive processing, which is attributed to strong SiC–NbC chemical interactions and improved microstructural features. Special emphasis was placed on the ability of the SiC matrix to chemically incorporate NbC particles, which is a critical prerequisite for the subsequent *introduction of NbC fibers – an avenue of ongoing research.* Such reinforcement is expected to enhance fracture toughness and damage resistance further. The results demonstrate that tailoring the microstructure through controlled NbC addition and optimised processing enables the design of SiC-based composites with improved mechanical performance.

## ACKNOWLEDGMENT

"Funded by the EU NextGenerationEU through the Recovery and Resilience Plan for Slovakia under the project No. 09I03-03-V04-00746."


## REFERENCES

[1] N.P. Padture, In Situ-Toughened Silicon Carbide, J. Am. Ceram. Soc. 77 (1994) 519–523

[2] F. Guillard, A. Allemand, J.D. Lulewicz, J. Galy, Densification of SiC by SPS-effects of time, temperature and pressure, J. Eur. Ceram. Soc. 27 (2007) 2725–2728

[3] M. Kostecki, M. Petrus, T. Płociński, A.R. Olszyna, Spark Plasma Sintering of Variable SiC α/β Ratio with Boron and Carbon Additions—Microstructure Transformation, Ceramics. 5 (2022) 1255–1268

[4] Y. Wang, S. Dong, X. Li, C. Hong, X. Zhang, Synthesis, properties, and multifarious applications of SiC nanoparticles: A review, Ceram. Int. 48 (2022) 8882–8913

[5] G.W. Lin, J.X. Liu, Y. Qin, G.J. Zhang, Low-temperature reactive sintering of carbon vacant high-entropy carbide ceramics with in-situ formed silicon carbide, J. Am. Ceram. Soc. 105 (2022) 2392–2398

[6] H. Liu, W. Sun, Y. Lu, S. Wei, High density NbB2-NbC composites: From controllable synthesis of NbB2-NbC composite powers to strengthening and toughening by adding SiC, J. Alloys Compd. 1017 (2025) 179054

[7] Y. Ma, Y.L. Li, H.Y. Yang, Y.Z. Wei, L. Liu, F. Qiu, Q.C. Jiang, The role of in-situ dual-phase NbB2 and NbC particles on the microstructure and toughening mechanisms of NiAl composites, Ceram. Int. 51 (2025) 31320–31331

[8] N. Ali, J. Li, L. Zhang, C. Zhang, H. Zhou, D. Liu, K. Sanaullah, Y. Nian, J. Cheng, Break the strength and ductility trade-off in novel NbC reinforced Fe40.5(CoCr)25Mn17.5Ni10Si5 high entropy alloy, Mater. Des. 239 (2024) 112752

# Silica cross-linking in alkali-activated $Si_3N_4$

Gianmarco Taveri[1,2], Guido de la Torre Olvera[1], Zuzana Netriova[2], Parisa Labib Shotorban[2], Matej Mičušik[3]

[1]*Centre of Advanced Materials and Applications (CEMA), SAV v.v.i., Dúbravská cesta 9, Bratislava (SK)*
[2] *Institute of Inorganic Chemistry (UACh), SAV v.v.i., Dúbravská cesta 9, Bratislava (SK)*
[3]*Institute of Polymers, SAV v.v.i., Dúbravská cesta 9, Bratislava (SK)*

## ABSTRACT

In the attempt to densify $Si_3N_4$ powder on drastically reduced temperatures, the alkali-activation process was utilized to activate the surface of the pristine silicon nitride by treating the material in a mild NaOH solution with a dissolve the oxide layer usually occurring on the particle's surface, and thus forming a dense amorphous sodium silicate phase covering the particles upon water evaporation. The dried product was then calcined at 750 °C to create the silica crosslink. In this study, we analysed the crosslinking process through a series of spectroscopic chemical analysis. It was found that the calcination dehydrates the sodium silicate to establish the silica 3D network, while the dehydroxilation creates a thin glassy strong phase connecting the $Si_3N_4$ particles.

**Keywords:** alkali-activation, low-temperature sintering, $Si_3N_4$, crosslinking

## INTRODUCTION

In response to the global demand for environmentally sustainable manufacturing, significant efforts are being made to develop processes that reduce emissions and energy consumption. Traditionally, ceramics are industrially produced through a conventional sintering process, often requiring temperatures exceeding 1000 °C, and thus far from aligning with net-zero carbon emission EU policies.

Silicon nitride ($Si_3N_4$) is a well-known material widely used in high-temperature and high-stress environments, particularly in industries such as aerospace, automotive and biomedical engineering. This is due to its exceptional combination of mechanical properties — including high elastic modulus, bending strength and fracture toughness, as well as chemical resilience, such as resistance to solid particle erosion and stability against most acidic and basic environments.

Although high-purity silicon nitride powders are commercially available, they typically contain a certain amount of silica ($SiO_2$), which can influence the material's behavior in basic media. Zhenta et al. [1] demonstrated that silicon nitride can undergo surface oxidation under normal oxygen pressure, forming a thin oxide film. In addition, when exposed to water vapor, silicon nitride undergoes chemical adsorption followed by hydrolysis, leading to the formation of silicon oxide and ammonia. These reactions underscore the importance of understanding surface chemistry and environmental interactions when evaluating the long-term performance of silicon nitride in biomedical or harsh industrial environments.

To promote an eco-sustainable fabrication route especially for bio-ceramic materials, alkali activation [2] has emerged as a promising alternative. In this approach, we propose using alkali activation to functionalize the surface of silicon nitride particles, potentially initiating a reaction pathway that yields a new class of alkali-activated ceramics. Such a process could represent a ground-breaking advancement in the development of next-generation healthcare materials.

Furthermore, this method is both cost-effective and environmentally friendly, aligning with global efforts toward greener and more efficient material processing.

## EXPERIMENTAL

The reagents employed for the slurry preparation and processing of the Alkali-activated materials (AAMs) were: silicon nitride ($Si_3N_4$, α-phase > 95 wt. %, $D_{90}$ = 0.5 μm, oxygen content < 2.0 wt. %, Ube Corporation, Tokyo, Japan), sodium hydroxide pellets as alkaline activator (purity 98 %, catalog no. P1313762130, $M_w$ = 40 g·mol$^{-1}$, Merck, Germany), and distilled water. The solution was prepared at a molarity of 0.35 M and a chemical modulus m=$SiO_2/Na_2O$=1. This value of m ensures maximum strength and crack-free calcined solid. The solid to liquid ratio defined as (Mass of dry slurry (g))/(Mass of wet slurry(g)) higher than 0.50 to ensure adequate slurry for avoiding crack in the bulk in both material after curing and calcination process. The slurry was stirred for 24 hours in a plastic cylindrical mold to obtain the desired bulk shape, while evaporating the water using a hot plate set at 100 °C. The slurry was then cured in an oven at 50 °C for 24 hours under air atmosphere. Following curing, the samples were further heated in the same oven at 150 °C to remove residual moisture. Subsequently, the samples were calcined at 750 °C for 3 hours (ramp up and down 10 °C min$^{-1}$) in air using a Clasic 0213 T furnace (Clasic CZ s.r.o., Řevnice, Czechia). The crystalline phases of the powder, alkali-activated and calcined samples were analyzed by X-ray diffraction (XRD) using an Empyrean diffractometer (Malvern Panalytical, United Kingdom) equipped with Cu Kα radiation (λ = 1.5406 Å) in a Bragg–Brentano configuration. Data were collected over a 2θ range of 10–80°, with a step size of 0.026° and a counting time of 50 s per step. The thermal evolution of the pristine powders, the alkali-activated materials and the calcined materials was examined through TGA/DTA thermal analysis up to 1200 °C in the air with a ramp of 10 °C/min, using an STA 449 F3 Jupiter (Netzsch Gerätebau GmbH, Germany). Disposable alumina crucibles were used for the measurements. Fourier Transform Infrared spectroscopy (FTIR) measurements were performed using a Nicolet 6700 spectrometer (Thermo Scientific, USA) equipped with IR source, KBr beamsplitter, and DTGS detector for mid- IR (MIR) region. The spectra were collected in the frequency range of 4000-400 cm$^{-1}$ with a resolution of 4 cm$^{-1}$. XPS signals were recorded using a Thermo Scientific Nexsa G2 Surface Analysis System (Thermo Fisher Scientific, UK) equipped with a micro-focused, monochromatic Al Kα X-ray source (1486.68 eV). An X-ray beam of 400 μm size was used. The spectra were acquired in the constant analyzer energy mode with a pass energy of 200 eV for the survey. Narrow regions were collected using the pass energy of 50 eV. Spectral calibration was determined by using the automated calibration routine and the internal Au, Ag and Cu standards supplied with the KAlpha system. The morphology of the microstructure was inspected through scanning electron microscopy (SEM) using a JEOL EVO 40 series electron microscope, equipped with detectors for backscattered electrons and X-rays.

## RESULTS

The microstructure of the alkali-activated (AA) and the calcined material possesses an intrinsic different morphology, as depicted in the SEM images in **Fig. 1**. The AA material shows the characteristic of a green-body, with a ragged surface and a wide range of porosity, calculated to be approx. 50 % using a mercury hydrometer and considering a mix of 96.5 $Si_3N_4$ and 3.5 % $SiO_2$ as theoretical density. At higher magnifications (50000x), the AA material shows the presence of an alkali-activation product, in the form of sodium silicate, embedding homogenously the pristine powder and connecting them with long strips. Once the material was calcined at 750 °C, a smoother polished surface was achieved, but never mirror-like. This is because of the pre-existent porosity, as visible in the pictures of the calcined material. Surprisingly, the microstructure of the calcined material appears amorphous, and the grains

became coarser. It is supposed that this glassy phase, growing during calcination, is due to the presence of sodium silicate modifying during calcination and thus inducing a grain coarsening.

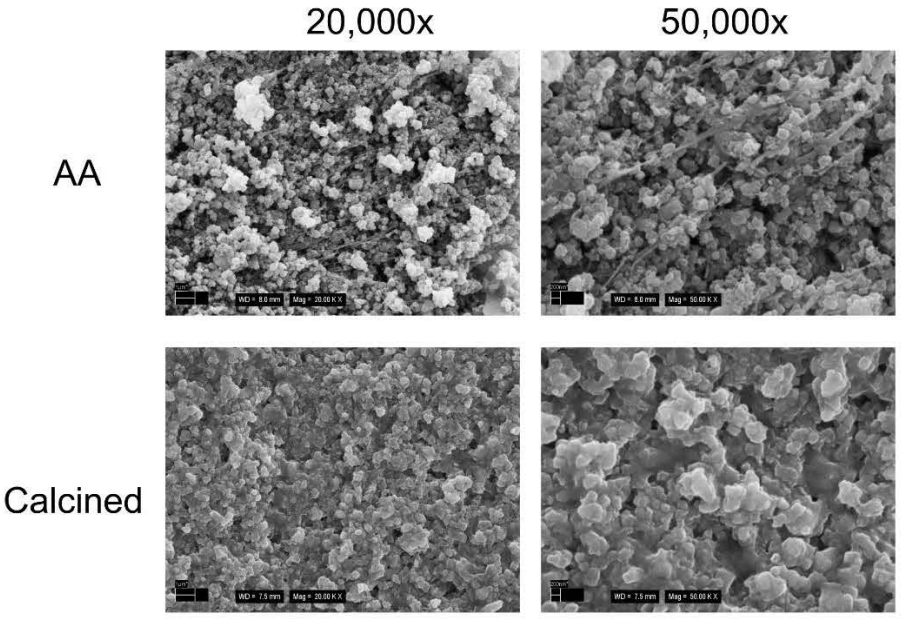


***Fig. 1*** *SEM images of the alkali-activated (AA) and calcined silicon nitride powder at different magnifications*

An in-depth characterization of the pristine powder, AA and calcined material was then carried out. **Fig. 2a** shows the TG-DTA thermal analysis conducted on the pristine powder and AA samples. The pristine powder does not show any weight loss, but only a sharp increase after 1200 °C due to powder oxidation. This reaction is identified with a large endothermic hump starting at 800 °C. The TG curve of the AA material shows two downward steps at 80 °C and 334 °C for a total weight loss of approx. 10 %, prior to soaring up at 900 °C. The DTA curve possesses an endothermic peak at 80 °C associated with the evaporation of the physical water, an intense exothermic peak at 334 °C, a less intense one at 546 °C of unclear origins and an exothermic shoulder at 712 °C. It is supposed that the first peak is associated with the dehydration reaction of the $Na_2O{\cdot}SiO_2{\cdot}nH_2O$ sodium silicate, as it is accompanied by a big weight loss in the TG curve [3]. The XRD patterns of the three samples do not show significant differences, except for minor peaks in the AA materials, which could not be fit through the database, and another minor peak in the calcined sample at approx. 21.7°, associated with the formation of cristobalite. This is a proof of a recrystallization reaction of the alkali-activated product which should happen around 650-700 °C according to a previous study of $Si_3N_4$ composite with an ex-situ alkali-activated matrix [4], in which a combeite phase was extensively formed. However, the DTA curves in this study look overall different from that study. Particularly, this peak seems to be displaced from the center of the cristobalite peak, usually happening at 21.8°. This is because the cristobalite is modified with sodium and therefore causing the peak to move to the left. The Rietveld refinement of the detected phases shows a predominance of α- $Si_3N_4$ phase (98.1 %wt) followed by β-$Si_3N_4$ phase (1.4 %wt), whilst the amount of formed cristobalite remains negligible (<1 %wt). FTIR spectroscopy of the three samples did not show significant information about the process of alkali-activation of the $Si_3N_4$ powder, as the two spectra (powder and AA) in **Fig. 2c** are almost identical. The AA material even show a less pronounced hump at 900-1000 $cm^{-1}$ related to the vibration of the Si-O bonds. This is because the alkali-activation dissolves the silica to form sodium silicate, which

goes on the surfaces of the slurry due to syneresis of the suspension, as proved by the huge amorphous halo at low 2θ angles in the XRD pattern of the upper surface of the calcined sample in **Fig. 2b**. Therefore, the grinding of the upper rugged surface of the AA green-body causes

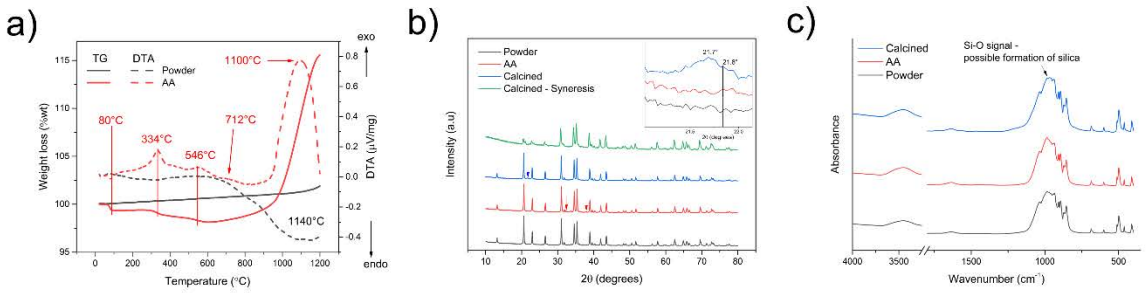


***Fig. 2** a) TG-DTA, b) XRD and c) FTIR of the $Si_3N_4$ powder, the alkali-activated $Si_3N_4$ (AA) and the calcined sample*

the elimination of the sodium silicate excess, which is a bless in disguise as it allows a more compact green-body with a very thin layer of sodium silicate covering the $Si_3N_4$ particles. The calcined material, on the contrary, shows again a Si-O hump, even more pronounced than the pristine powder, suggesting a possible formation of silica or at least more Si-O bonds during calcination. Because the cristobalite content is below 1 %wt according to the XRD refinements, whereas the pristine powder possesses a $SiO_2$ content of approx. 2 %wt (according to specifications), the calcination must induce the formation of Si-O in the form of an amorphous phase not detectable through XRD. The DTA of the green body also shows a big endothermic hump starting at 900 °C and ending at 1100 °C related to the extensive formation of $Si_2N_2O$ phase [5]. Therefore, a calcination temperature below 900 °C is desirable.

XPS spectroscopy is a useful technique to perform an accurate analysis of the material's chemistry, allowing to construct a full picture of the samples. The XPS measurements performed on the three samples are reported in **Fig. 3** with the single Si2p, N1s and O1s core-levels, as they are the most significant. The XPS spectrum of the pristine powder presents the typical fingerprints of the $Si_3N_4$ material [6], with a strong Si-N signal at 397.5 eV in the N1s core-level, and at 101.5 eV in the Si2p core-level, while the O1s core-level presents only the Si-O contribution at 532.4 eV due to the surface oxide layer. The Si2p core-level certifies the oxidation with a small signal at 103.0 eV. Its concentration in at % was calculated to be 5.3 at %, but XPS is not a bulk elemental analysis so the concentrations are relative. Notice that the N1s also features a small signal at approx. 400 eV, which regards the presence of silicon oxynitride (Si-N-O) possibly on the particles surface. The AA material possesses the same features, with the only difference that the O1s core-level presents a meaningful signal at 531.4 eV associated with the Na-Si=O belonging to the alkali-activated sodium silicate product (the amorphous strips in **Fig. 1**). This core-level also shows a contribution at 534 eV associated with the Si-OH hydrated form of the sodium-silicate [7], dimly present in the pristine powder as well, due to moisture absorption on the oxide layer. In the calcined sample, the Si2p core-level presents a very pronounced contribution from the Si-O bond at 103 eV accompanied with the signal at 531 eV in the O1s core-level associated with the Na-Si-O product, but this core-level does not show any presence of the Si-OH hydrated product. This implies that the small exothermic peak at 546 °C in Figure 2a is the reaction of sodium silicate dehydroxilation of the Si-OH. This reaction enables the structuration of the silica 3D network with large content of O-Si-O bonds, as shown in the Si2P core-level and thus bridging with the surface of the pristine powder. Noticed that the N1s core-level of the calcined sample still presents the Si-N-O feature at 400 eV meaning that the bridging can also be an amorphous silicon oxynitride. The glass

transition induces the formation of a glassy silica phase, thereby explaining the discrepancy in the detected crystalline silica in the XRD measurements.

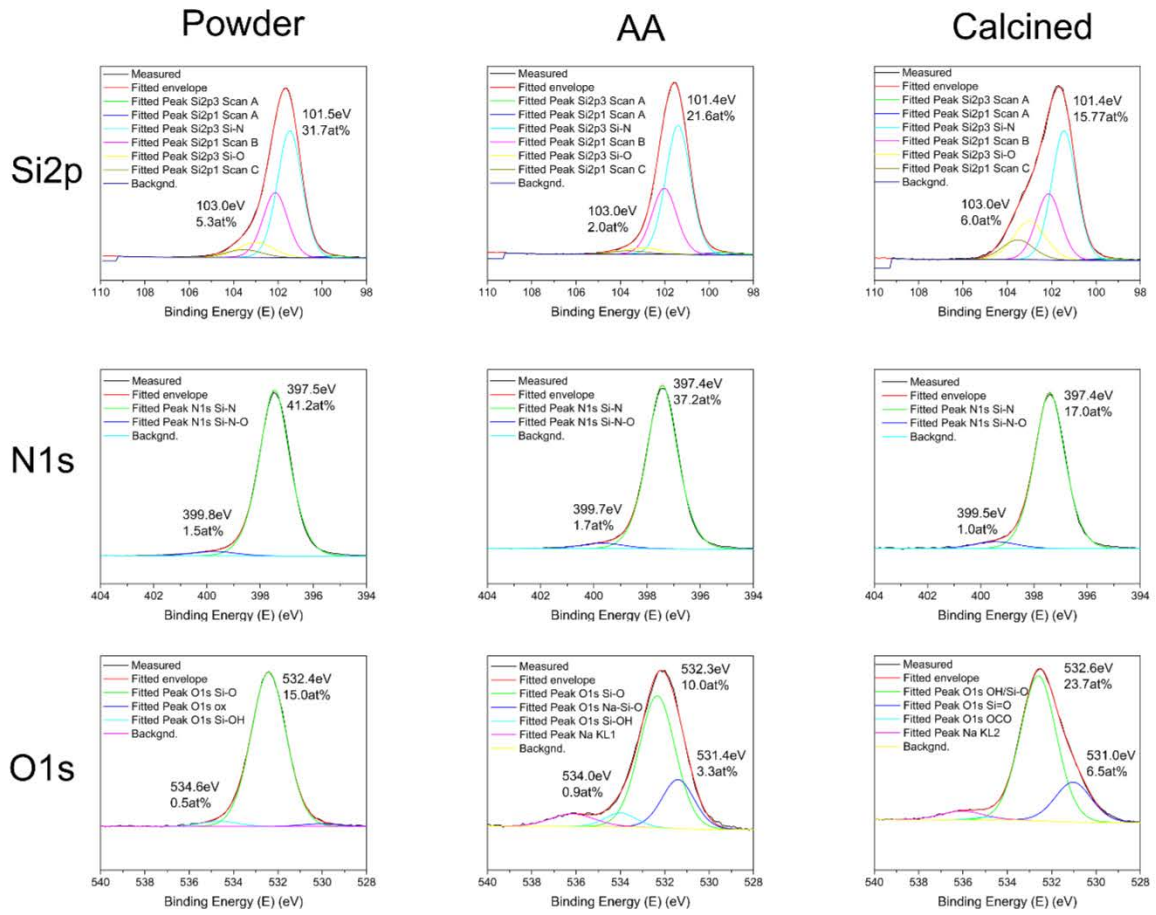


***Fig. 3*** *Si2p, N1s and O1s core-levels of the XPS spectroscopy measurement performed on the $Si_3N_4$ powder, alkali-activated (AA) material and the calcined material*

## CONCLUSIONS

In this study, the alkali-activation method was used to functionalize the $Si_3N_4$ particles surface in order to densify the powder at the temperature of 750 °C, by mixing the powder with a NaOH solution having enough sodium to form a chemical modulus m=$SiO_2/Na_2O$=1 with the $SiO_2$ on the particles surface. After water evaporation, a dense, malleable slurry is formed, followed by a dry, green body. A calcination at 750 °C for 3h complete the method. The process of silica cross-linking was studied through SEM, TG-DTA, XRD, FTIR and XPS. The micrographs show that after alkali-activation, the powder is homogenously embedded by the sodium-silicate, while the calcination induces a coarsening of the grains. The thermal analysis reveals that the green body undergoes a double exothermic reaction at 335 °C and 546 °C, corresponding to dehydration and the dehydroxylation reaction of the sodium-silicate, respectively. The FTIR shows the formation of silica in the calcined material, but the XRD detected only a small peak related to cristobalite; therefore, the crosslinked silica must be mainly an amorphous glassy phase. The XPS results confirmed that the major difference between the alkali-activated green body and the calcined ceramic lies in the level of hydration (Si-OH vs. Si-O), while also suggesting that crosslinking could be possible through a Si-O-N network.

**ACKNOWLEDGMENT**

This work was funded by the EU NextGenerationEU through the Recovery and Resilience Plan for Slovakia under the project No. 09I03-03-V04-00287, and by the APVV agency, project No. APVV-23-0474.

**REFERENCES**

[1] Z. Ni, J. Jiang, X. Yang, X. Yang, Z. Zhou, Q. He, Surface characterization of silicon nitride powder and electrokinetic behavior of its aqueous suspension, Ceram. Int. 46 (2020) 9530–9537. https://doi.org/10.1016/j.ceramint.2019.12.215

[2] J.L. Provis, A. Palomo, C. Shi, Advances in understanding alkali-activated materials, Cem. Concr. Res. 78 (2015) 110–125. https://doi.org/10.1016/j.cemconres.2015.04.013

[3] J. Felsche, B. Ketterer, R.L. Schmid, Thermal Study on Sodium Silicate Hydrates Na2[SiO2(OH)2]nH2O (n=4,5,6,7). Phase Relations and Decomposition Characteristics Under Open-System Conditions, Thermochim. Acta. 88 (1985) 443–451

[4] G.M.O. de la Torre, M. Tatarková, Z. Netriová, M. Barlog, L. Bertolla, M. Hnatko, G. Taveri, Applying the Alkali-Activation Method to Encapsulate Silicon Nitride Particles in a Bioactive Matrix for Augmented Strength and Bioactivity, Materials (Basel). 17 (2024). https://doi.org/10.3390/ma17020328

[5] Q. Tong, J. Wang, Z. Li, Y. Zhou, Low-temperature synthesis/densification and properties of Si2N2O prepared with Li2O additive, J. Eur. Ceram. Soc. 27 (2007) 4767–4772. https://doi.org/10.1016/j.jeurceramsoc.2007.04.004

[6] J.R. Shallenberger, D.A. Cole, S.W. Novak, Characterization of silicon oxynitride thin films by x-ray photoelectron spectroscopy, J. Vac. Sci. Technol. A Vacuum, Surfaces, Film. 17 (1999) 1086–1090. https://doi.org/10.1116/1.582038

[7] Y. Zhang, L. Zhu, L. Chen, L. Liu, G. Ye, Influence of Magnesia on Demoulding Strength of Colloidal Silica-Bonded Castables, Rev. Adv. Mater. Sci. 58 (2019) 32–37. https://doi.org/10.1515/rams-2019-0008

*Silikátnik 2025, Special issue*

„PROCESSING AND PROPERTIES OF ADVANCED CERAMICS AND GLASSES"

*Published by:* Slovak Silicate Scientific-Technological Society
Kocel'ova 15
815 94 Bratislava
Slovakia

*December 2025*

*Reviewers:* prof. Ing. Marián Janek, PhD.
Ing. Ondrej Hanzel, PhD.
Ing. Martin Michálek, PhD.

*Edited by:* Ing. Jana Valúchová, PhD.

*Graphic design:* Ing. Jana Valúchová, PhD.

*Cover photo:* Ing. Ondrej Hanzel, PhD.

ISBN 978-80-975243-0-2

ISBN 978 - 80 - 975243 - 0 - 2